

# A stochastic force model for a finite-size spherical particle in turbulence

Yuqi Wang<sup>a</sup>, Ruifeng Hu<sup>a,\*</sup>

<sup>a</sup>Center for Particle-Laden Turbulence, Key Laboratory of Mechanics on Disaster and Environment in Western China, Ministry of Education, College of Civil Engineering and Mechanics, Lanzhou University, Lanzhou, 730000, Gansu, China

## ARTICLE INFO

### Keywords:

Particle-laden flow  
Finite-size particle  
Fluid force modeling  
Turbulence

## ABSTRACT

Predicting particle-laden flows requires accurate fluid force models. However, a reliable particle force model for finite-size particles in turbulent flows remains lacking. In the present work, a fluid force model for a finite-size spherical particle in turbulence is developed by simulating turbulent flow past a fixed spherical particle using particle-resolved direct numerical simulation (PRDNS). Our simulation demonstrates that turbulence increases the mean drag force of the particle, which is consistent with previous studies. By correlating the DNS data as functions of the Reynolds number of particles, the ratio of the particle-to-turbulence scale, and the intensity ratio of the turbulence, an empirical correlation for the mean drag force is obtained. Furthermore, we find that the fluctuations of both the drag and lateral forces follow the Gaussian distribution. Consequently, the temporal variations of the fluctuating drag and lateral forces are modeled using a stochastic Langevin equation. Empirical correlations of the fluctuation intensities and time scales involved in the stochastic model are also determined from the DNS data. Finally, we simulate the movement of a finite-size particle in turbulence and the dispersion of particles in a turbulent channel flow to validate the proposed model. The proposed fluid force model requires the mean flow velocity, the kinetic energy of the turbulence, and the dissipation rate of the turbulence as inputs, which makes it well suited for combination with the Reynolds-averaged Navier-Stokes (RANS) approach.

## 1. Introduction

Particle-laden flows are ubiquitous in nature and engineering applications, such as sediment transport, dust storms, fluidized bed reactor flow, and the spread of haze pollutants in cities. For decades, numerical methods for particle-laden flows have been greatly developed, and numerical simulation has become a powerful tool in both fundamental research and practical processes. Depending on the different levels of assumptions, the numerical methods for particle-laden flows can be roughly classified as the Eulerian two-fluid method, the Lagrangian particle method, and the fully resolved method (Drew, 1983; Elghobashi, 1994; Crowe, Troutt and Chung, 1996; Loth, 2000; Eaton, 2009; Wang, 2009; Balachandar and Eaton, 2010; Yu and Shao, 2010; Fox, 2012; Subramaniam, 2013; Tenneti and Subramaniam, 2014; Kuerten, 2016; Maxey, 2017; Elghobashi, 2019; Brandt and Coletti, 2022; Fox, 2024; Schneiderbauer, 2024). The prediction accuracy of particle-laden flows is critically dependent on the fluid force models used in numerical simulations (Michaelides, 1997, 2003; Loth and Dorgan, 2009).

The point-particle method is a widely used approach based on the Lagrangian framework, which has a long history in particle-laden flow simulations (McLaughlin, 1994; Balachandar, 2009; Eaton, 2009; Soldati and Marchioli, 2009; Kuerten, 2016). In this method, particles are modeled as infinitesimal points with finite mass and momentum, and there exists an exact theory for particle motion in the Stokes flow regime at very small particle Reynolds numbers (Tsai, 1957; Gatignol, 1983; Maxey and Riley, 1983; Tsai, 2022). The fluid forces exerted on a spherical particle include the Stokes drag force, the Basset history force, the added mass force, and the pressure gradient force. With a large particle-to-fluid density ratio, it is usually assumed that the drag force is the most dominant and other force terms can be neglected (Armenio and Fiorotto, 2001). At a finite particle Reynolds number, empirical correlation for the drag force is commonly leveraged, *e.g.* the Schiller-Naumann (S-N) drag correlation (Schiller and Naumann, 1933). The point-particle method requires that the particle size is generally much smaller than the smallest scale of turbulence, *i.e.*, the Kolmogorov length scale. However, for a finite-size particle whose size is larger than the Kolmogorov length

\*Corresponding author

✉ [hurf@lzu.edu.cn](mailto:hurf@lzu.edu.cn) (R. Hu)

ORCID(s): 0000-0001-7105-2703 (Y. Wang); 0000-0002-2505-5433 (R. Hu)

scale, the effect of small-scale turbulent motions around the particle may lead to an unreasonable prediction of the particle force with the point-particle method.

In the last three decades, particle-resolved or fully resolved direct numerical simulation has become a vital approach to resolving the flow around particles directly and accurately predicting particle-laden flows. Several different particle-resolved direct numerical simulation (PRDNS) approaches have been developed, such as the immersed boundary (IB) method (Mittal and Iaccarino, 2005; Uhlmann, 2005; Luo, Wang, Fan and Cen, 2007; Breugem, 2012; Kempe and Fröhlich, 2012; Zhou and Fan, 2014; Tao, Zhang, Guo and Wang, 2018; Huang and Tian, 2019; Wang, Vanella and Balaras, 2019; Verzicco, 2023; Mittal and Seo, 2023), the distributed Lagrange multiplier (DLM)/fictitious domain approach (Glowinski, Pan, Hesla and Joseph, 1999; Glowinski, Pan, Hesla, Joseph and Periaux, 2001; Yu and Shao, 2007, 2010), and others. PRDNS have been widely used to obtain high-fidelity simulation data, which is greatly helpful in studying particle transport in turbulent flows (Uhlmann, 2008; Shao, Wu and Yu, 2012; Kidanemariam, Chan-Braun, Doychev and Uhlmann, 2013; Picano, Breugem and Brandt, 2015; Luo, Hu, Wu and Fan, 2017; Vowinckel, Withers, Luzzatto-Fegiz and Meiburg, 2019; Costa, Brandt and Picano, 2020; Vowinckel, Zhao, Zhu and Meiburg, 2023; Peng, Wang and Chen, 2024), sediment transport (Ji, Munjiza, Avital, Ma and Williams, 2013; Ji, Munjiza, Avital, Xu and Williams, 2014; Kidanemariam and Uhlmann, 2014a,b; Vowinckel, Jain, Kempe and Fröhlich, 2016; Kidanemariam and Uhlmann, 2017; Mazzuoli, Blondeaux, Vittori, Uhlmann, Simeonov and Calantoni, 2020; Scherer, Uhlmann, Kidanemariam and Krayer, 2022; Zhu, Hu, Lei, Shen and Zheng, 2022; Schwarzmeier, Rettinger, Kemmler, Plewinski, Núñez-González, Köstler, Rüde and Vowinckel, 2023), turbulence modulation by particles (Pan and Banerjee, 1996; Vowinckel, Kempe and Fröhlich, 2014; Vreman, 2016; Peng, Ayala and Wang, 2019, 2020; Costa, Brandt and Picano, 2021; Yu, Xia, Guo and Lin, 2021; Oka and Goto, 2022; Peng, Sun and Wang, 2023; Balachandar, Peng and Wang, 2024), and developing particle force models (Hill, Koch and Ladd, 2001; Van der Hoef, Beetstra and Kuipers, 2005; Cate and Sundaresan, 2006; Beetstra, van der Hoef and Kuipers, 2007; Zeng, Najjar, Balachandar and Fischer, 2009; Tennesi, Garg and Subramaniam, 2011; Homann, Bec and Grauer, 2013; Tang, Peters, Kuipers, Kriebitzsch and van der Hoef, 2015; Zhou and Fan, 2015a,b; Akiki, Jackson and Balachandar, 2017a; Akiki, Moore and Balachandar, 2017b; Balachandar, Moore, Akiki and Liu, 2020; Seyed-Ahmadi and Wachs, 2020; Zhang, Jiang, Chen, Yu and Zhou, 2020; Tavanashad, Passalacqua and Subramaniam, 2021; Seyed-Ahmadi and Wachs, 2022; Xia, Yu, Pan, Lin and Guo, 2022; Cheng and Wachs, 2023a,b; Peng and Wang, 2023; van Wachem, Elmetikawy and Chéron, 2024; Xia, Lin, Guo and Yu, 2024).

Despite its high accuracy, conducting large-scale simulations of particle-laden flows with PRDNS remains prohibitively costly. Therefore, it is necessary to develop reliable particle force models that can be integrated with cost-effective Reynolds-averaged Navier-Stokes (RANS) or large-eddy simulation (LES) techniques for turbulent flows. Various studies have been conducted on particle force models utilizing PRDNS data. However, a considerable proportion of these models focus on laminar flows rather than turbulent flows, which substantially limits their applicability in numerous practical situations. Studies have been conducted on the impact of turbulence on the mean particle drag force, while models for the instantaneous drag force are significantly deficient. In the following, we will review the current progress of the turbulence effects on the drag force of a finite-size particle and the prediction models.

### 1.1. Effects of turbulence on the drag force of a finite-size particle and models

Some studies investigated the influence of turbulence on particle drag. Bagchi and Balachandar (2003) investigated the influence of freestream isotropic turbulent flow on the drag and lift forces exerted on a spherical particle by PRDNS. Their findings indicated that freestream turbulence does not have a significant or systematic influence on the time-averaged mean drag, and the standard empirical drag formula, based on the instantaneous or mean relative velocity, may accurately predict the mean drag with reasonable accuracy. The prediction accuracy of instantaneous drag reduces as the particle size increases. For smaller particles, the standard drag law effectively captures low-frequency oscillations of particle drag; however, for larger particles, a notable discrepancy arises even in the low-frequency component. Burton and Eaton (2005) studied the interaction between a fixed particle and the decaying homogeneous isotropic turbulence by PRDNS. They found that the Lagrangian point-particle equation of motion underpredicts the particle root mean square (RMS) force, and the RMS force errors between the PRDNS results and those predicted by the Lagrangian particle equation of motion are between 15% and 30%. Zeng, Balachandar, Fischer and Najjar (2008) conducted a PRDNS investigation on the force of a single fixed finite-size particle in turbulent channel flow, with the particle positioned at various wall-normal locations. It was found that when the particle is away from the viscous sublayer, the instantaneous drag is accurately captured by the standard drag law; in contrast, the particle drag is underestimated when the particle is in the buffer layer. Kim and Balachandar (2012) performed PRDNS of a particle in freestream

turbulence. They stated that the standard drag law defined with uniform flow simulation can accurately predict particle drag when turbulent intensity is sufficiently low (below 5%), while flow non-uniformity substantially influences the forces acting on a finite-size particle as turbulent intensity increases, a factor often overlooked in the context of small particles. They suggested that both deterministic and stochastic components must be incorporated into the particle force model to accurately predict the motion of finite-size particles in turbulent flows.

In addition, several studies proposed empirical formulas for particle drag considering the turbulence effect. [Brucato, Grisafi and Montante \(1998\)](#) conducted experiments to quantify the drag coefficient of particles in the Couette-Taylor turbulence. They determined that particle drag depends on particle size and turbulence intensity. Turbulence pulsation can markedly increase particle drag for larger particles, although it exerts no impact on the drag force for smaller particles. They proposed a correlation for predicting the effect of freestream turbulence on the mean drag coefficients of intermediate-sized particles,

$$\Delta C_D = A (D_p/\eta)^3, \quad (1)$$

where  $\Delta C_D = (C_D - C_{D0})/C_{D0}$  is the relative drag coefficient increment,  $C_D$  is the mean particle drag coefficient in a turbulent flow,  $C_{D0}$  is the particle drag coefficient from the standard S-N drag law ([Schiller and Naumann, 1933](#))

$$C_{D0} = C_D^{SN} = \frac{24}{Re_p} \left(1 + 0.15 Re_p^{0.687}\right), \quad (2)$$

$D_p/\eta$  is the ratio of particle diameter  $D_p$  to the Kolmogorov length scale  $\eta$ , and the constant  $A = 8.76 \times 10^{-4}$ .

[Homann et al. \(2013\)](#) examined the influence of turbulence on the drag force of a fixed finite-size particle through PRDNS. Their findings indicate that the mean particle drag increases with increasing turbulence intensity, and this enhancement is significantly greater than the predictions provided by the standard drag law. They proposed two correlations:

$$\Delta C_D = 0.18 I^2 Re_p Re_L^{1/2}, \quad (3)$$

and

$$\Delta C_D = \frac{0.45 Re_p^{0.687}}{1 + 0.15 Re_p^{0.687}} I^2, \quad (4)$$

in which  $I = u_{rms}/U_s$  is the relative turbulent intensity ( $u_{rms}$  is turbulent fluctuation velocity,  $U_s$  is the magnitude of mean particle-to-fluid slip velocity),  $Re_p = U_s D_p/\nu$  is the particle Reynolds number ( $\nu$  is fluid kinematic viscosity), and  $Re_L = u_{rms} L/\nu$  is the integral scale Reynolds number of turbulence ( $L = u_{rms}^3/\varepsilon$ ,  $\varepsilon$  is the mean kinetic energy dissipation rate).

[Peng and Wang \(2023\)](#) performed PRDNS to investigate the mechanism and model of drag enhancement in a finite-size particle in an anisotropic turbulent flow. They found that large-scale turbulence increases particle drag by enhancing the pressure drop on the particle surface, whereas small-scale turbulence improves the mixing of high- and low-speed flow at the particle boundary layer, consequently intensifying the viscous stresses on the particle surface. They additionally offered a model for the enhancement of particle drag in turbulent flow, taking into account the anisotropy of the flow, as

$$\Delta C_D = 0.06 \beta^{1.4} I^{0.5} Re_p^{-0.1} (D_p/\eta)^{0.9}, \quad (5)$$

where  $\beta = \langle u'_1 \rangle / (\langle u'_2 \rangle \langle u'_3 \rangle)^{0.5}$  is the anisotropy parameter of turbulence ( $\langle u'_1 \rangle$ ,  $\langle u'_2 \rangle$  and  $\langle u'_3 \rangle$  are the component-wise RMS velocities in three directions).

[Wang, Lei, Zhu and Zheng \(2023\)](#) explored the drag force on the saltating particles over an erodible particle bed in a turbulent open channel flow using PRDNS. Their findings indicate that the mean drag force on the saltating particles is related to the square of the vertical particle velocity, and a drag force correlation based on the S-N drag law was established using data fitting, which is

$$\Delta C_D = \frac{40(u_{p,y}/u_{p,0})^2 + 27}{Re_p} - 1, \quad (6)$$

**Table 1**

Empirical correlations for the mean particle drag coefficient in turbulence.

	Drag model	$Re_p$	$I$	$D_p/\eta$
Brucato et al. (1998)	Eqn. (1)	< 40	0.05, 0.5	2.5 ~ 30
Homann et al. (2013)	Eqns. (3) and (4)	20 ~ 400	0.05 ~ 0.6	1.1 ~ 44
Peng and Wang (2023)	Eqn. (5)	100 ~ 300	0.17 ~ 0.27	6.89 ~ 22.1
Wang et al. (2023)	Eqn. (6)	< 80	/	/
Xia et al. (2022)	Eqns. (7), (8) and (9)	< 227	0.1 ~ 30	/
Xia, Lin, Guo and Yu (2023)	Eqn. (10)	< 227	0.1 ~ 30	/

where  $u_{p,y}$  is the vertical particle velocity at the height of  $y_p$  and  $u_{p,0}$  is the initial vertical particle velocity.

Xia et al. (2022) proposed several mean drag correlations for particles in upward particle-laden turbulent channel flows from the PRDNS data of Yu et al. (2021). They are,

$$\Delta C_D = 0.448 [k/U_s^2 - (k/U_s^2)_0]^{0.525}, \quad (7)$$

$$\Delta C_D = \begin{cases} 1.25 \frac{0.15 Re_m^{0.687}}{1 + 0.15 Re_m^{0.687}} I^2, & I < 1, \\ 1.64 \frac{0.15 Re_m^{0.687}}{1 + 0.15 Re_m^{0.687}} I^{0.687}, & I > 50, \end{cases} \quad (8)$$

and

$$\Delta C_D = 1.32 \frac{0.15 Re_m^{0.687}}{1 + 0.15 Re_m^{0.687}} (I - I_0)^{1.1}, \quad (9)$$

where  $k$  is the turbulence kinetic energy (TKE),  $(k/u_s^2)_0 = 0.0125 + 2.15\phi_s - 5.83\phi_s^2$  is the particle-induced TKE ( $\phi_s$  is the particle volume fraction),  $Re_m = \phi_f Re_p$  is the particle Reynolds number considering the effect of particle volume fraction ( $\phi_f$  is the fluid volume fraction), and  $I_0 = [2(k/u_s^2)_0/3]^{1/2}$  is the particle-induced turbulent intensity.

Also based on the PRDNS data of Yu et al. (2021), Xia et al. (2023) developed another particle drag correlation, as

$$\Delta C_D = 0.125\beta^{0.365} (I - I_0)^{0.574} Re_m^{-0.647} (D_p/\eta)^{1.581}, \quad (10)$$

where  $\beta$  is the anisotropy parameter of the turbulence, which is the same as that in equation 5.

Table 1 summarizes the range of parameters of the studies on the particle drag force models mentioned above.

## 1.2. Stochastic models in particle-laden flow

Employing PRDNS to deal with practical particle-laden flows remains impossible due to the enormous computational cost. RANS or LES are more practical alternatives for computing fluid flows in actual applications. Nevertheless, throughout the averaging and filtering procedures in RANS and LES, subgrid-scale (SGS) flow information is filtered out and absent, necessitating modeling its effects on the particle. The existing particle SGS models can be classified into two groups, *i.e.* structural models and stochastic models (Marchioli, 2017; Pozorski, 2017). The structural models aim to reconstruct the entire SGS flow velocity field (Kuerten, 2006; Shotorban and Mashayek, 2006a; Marchioli,



Salveti and Soldati, 2008a,b; Ray and Collins, 2014; Park, Bassenne, Urzay and Moin, 2017; Zhou, Wang and Jin, 2018; Bassenne, Esmaily, Livescu, Moin and Urzay, 2019; Zhou, Wang, Yang and Jin, 2020; Hausmann, Evrard and van Wachem, 2023a,b). The stochastic models try to retrieve some stochastic characteristics of the SGS flow field using stochastic methods (Wang and Squires, 1996; Fede and Simonin, 2006; Shotorban and Mashayek, 2006b; Berrouk, Laurence, Riley and Stock, 2007; Pozorski and Apte, 2009; Jin, He, Wang and Zhang, 2010; Cernick, Tullis and Lightstone, 2015; Minier, 2015; Innocenti, Marchioli and Chibbaro, 2016; Tanière and Arcen, 2016; Tenneti, Mehrabadi and Subramaniam, 2016; Innocenti, Fox, Salvetti and Chibbaro, 2019; Sabelnikov, Barge and Gorokhovski, 2019; Lattanzi, Tavanashad, Subramaniam and Capecelatro, 2020; Knorps and Pozorski, 2021; Lo, Bons, Yao and Capecelatro, 2022; Roustas, Lessani and Ahmadi, 2024). In this work, we focus on the stochastic method due to its capability in particle force modeling.

Two distinct stochastic modeling approaches have emerged to achieve this purpose. The first approach used the Lagrange stochastic technique to simulate the velocity of the unresolved flow experienced by particles, grounded in the point-particle framework and referred to as the flow Lagrangian stochastic model. This method utilizes statistical flow characteristics obtained from RANS or LES to generate instantaneous flow velocities encountered by particles via a stochastic model in the Lagrangian framework. The flow Lagrange stochastic methods can be classified into discontinuous random walk models (DRW) and continuous random walk models (CRW). The DRW model posits that when a particle traverses an eddy during a specific duration, the fluctuating velocity of the flow within that eddy remains constant. Upon moving to the subsequent eddy, a new fluctuating velocity is established, independent of the prior period (Gosman and Ioannides, 1983; Bocksell and Loth, 2001; Dehbi, 2008; Mofakham and Ahmadi, 2020). The CRW model connects the current velocity fluctuation of the flow field to that of the preceding time step through a Markov chain constructed from the Langevin equation (Wang and Stock, 1992; Bocksell and Loth, 2006), offering a continuous variation of the fluid velocity fluctuation and thus deemed more realistic than the DRW model. The CRW model has been widely used in simulating particle dispersion in turbulent flows (Bocksell and Loth, 2006; Dehbi, 2008, 2010; Mofakham and Ahmadi, 2019, 2020; Jaiswal, Bui and Rutschmann, 2022; Li, Shi and Yu, 2023).

The other approach for modeling the impacts of the unresolved flow originates at the particle level and incorporates stochastic models for particle position, velocity, or acceleration based on the Langevin equation, referred to as the particle Lagrangian stochastic model. For example, Garzó, Tenneti, Subramaniam and Hrenya (2012) proposed a model for particle acceleration by modeling particle velocity fluctuation as a Langevin model to account for the stochastic nature of neighbor particle effects in the Stokes flow regime. Tenneti et al. (2016) extended the particle acceleration Langevin model proposed by Garzó et al. (2012) to moderate particle Reynolds numbers by PRDNS. Esteghamatian, Euzenat, Hammouti, Lance and Wachs (2018) proposed a stochastic formulation for the drag of particles considering the effects of the filtered microstructure of turbulence through PRDNS. Lattanzi et al. (2020) introduced a detailed description of stochastic methods that can be used in Eulerian-Lagrangian simulations to account for fluctuations in the neighbor-induced drag force of the particles, including the Langevin equation for the position, velocity, and fluctuating drag force of the particles. Lattanzi, Tavanashad, Subramaniam and Capecelatro (2022) developed a Langevin drag force model that treats neighbor-induced drag fluctuations as a stochastic force within the Eulerian-Lagrangian framework. They closed the model with the integral timescale for the fluctuating hydrodynamic force and the standard deviation in drag.

### 1.3. The present work

The studies mentioned above indicate that while there are some correlations for the mean particle drag considering the effects of turbulence, no model for instantaneous particle force is available for direct application to simulate the motion of finite-size particles in turbulence. To fill this gap, we perform PRDNS of a finite-size particle in turbulence across a wide range of turbulence and particle parameters and offer a stochastic model for the instantaneous particle drag and lateral force, accounting for the effects of turbulence.

The rest of the paper is organized as follows: §2 introduces the simulation methods employed in this work, including PRDNS, turbulent forcing, and particle wake elimination methods. In §3, the new correlations for the mean particle drag and the stochastic models for the fluctuating particle drag and the lateral forces are given. In §4, the proposed model is validated by simulating the motion of a finite-size particle in a turbulent flow and the dispersion of particles in a turbulent channel flow, respectively. Finally, the main conclusions are drawn in §5.

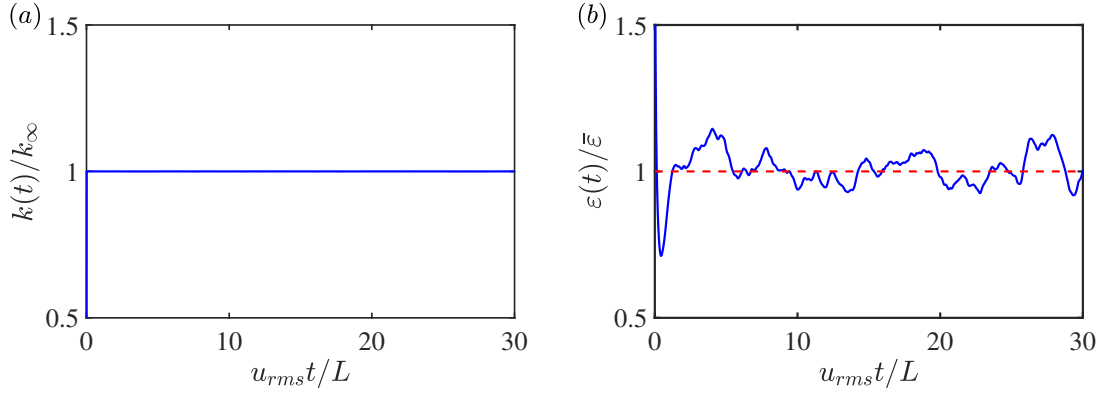


**Figure 1:** Time variations of the spatially averaged TKE (a) and TDR (b) of the turbulent flow using the turbulence forcing method. Here  $k_\infty = (3/2)u_{rms}^2$  is the target TKE,  $u_{rms}$  is the target rms value of turbulent velocity, and  $L = u_{rms}^3/\bar{\epsilon}$  is the integral length scale. Here  $\langle \cdot \rangle$  represents temporal averaging.

## 2. Simulation methods

### 2.1. Particle-resolved direct numerical simulation (PRDNS)

This study employs PRDNS to evaluate the particle-fluid interaction to quantify the force exerted by the fluid on the particle. The governing equations of fluid flow are the three-dimensional Navier-Stokes equations for incompressible flow

$$\frac{\partial \mathbf{u}}{\partial t} + \nabla \cdot (\mathbf{u}\mathbf{u}) = -\nabla p + \frac{1}{Re} \nabla^2 \mathbf{u} + \mathbf{f}_{IB} + \mathbf{f}_{TF}, \quad (11)$$

and the continuity equation,

$$\nabla \cdot \mathbf{u} = 0. \quad (12)$$

where  $\mathbf{u}$  is the fluid velocity,  $p$  is the fluid pressure,  $Re$  is the Reynolds number,  $\mathbf{f}_{IB}$  is the immersed-boundary volumetric force of the particle on the flow, and  $\mathbf{f}_{TF}$  is the turbulence forcing term. The numerical solver used in the PRDNS study is the opensource code CP3d (Gong, Wu, An, Zhang and Fu, 2023). The fractional step approach from Kim and Moin (1985) is utilized for equations (11) and (12) to ensure that the flow velocity field remains divergence-free. The second-order Adams-Bashforth scheme is employed for the convection term, while the Crank-Nicolson scheme is adopted for the viscous term in the time advancement. The second-order central difference scheme is used for spatial discretization. The efficacy of the PRDNS code has been thoroughly validated (Gong et al., 2023).

The interaction between a particle and fluid flow is computed using the direct-forcing immersed boundary (IB) approach developed by Uhlmann (2005), where a Cartesian grid is employed in the flow solver, and the particle is represented by Lagrangian surface points. The IB method enforces the non-slip boundary condition on the particle surface by including  $\mathbf{f}_{IB}$  on the right-hand side of equation (11), which is determined by the difference in velocity between the Lagrangian point and the interpolated flow velocity. The interpolation between the Lagrangian points and the Eulerian flow field is performed using a regularized Dirac delta function (Roma, Peskin and Berger, 1999). More specifically, the IB force  $\mathbf{f}_{IB}$  is calculated using a multidirect forcing scheme (Luo et al., 2007; Breugem, 2012). This method incorporates an external iterative process to determine the interaction force  $\mathbf{f}$  between the particle and the flow with the direct forcing IB method and can reduce the error associated with the diffused interaction between Lagrangian points and the flow field, thus improving the accuracy of the particle-flow interaction computation.

### 2.2. Turbulence forcing method

To accurately determine the relationship between the forces of the particle and the turbulence, a statistically stationary background turbulent-flow field must be generated and evolved. However, a turbulent flow without mean shear, such as homogeneous and isotropic turbulence (HIT), will decay over time in the absence of external energy

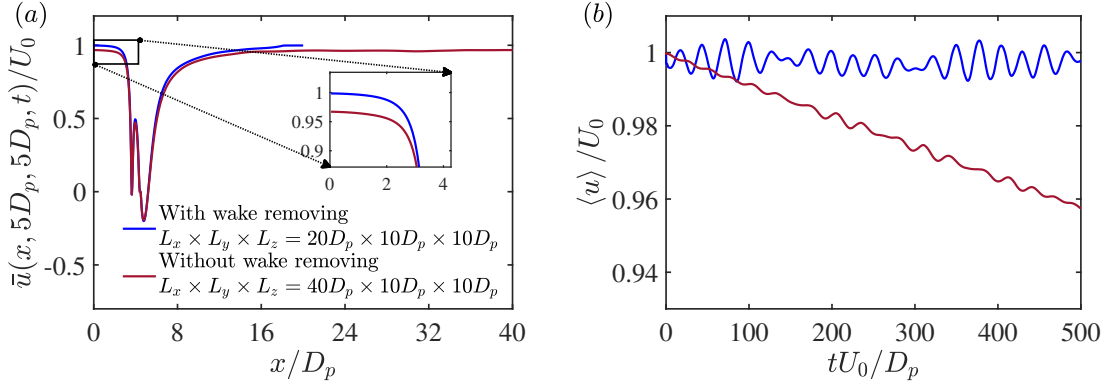


**Figure 2:** (a) The temporal mean streamwise flow velocity at the central line along the streamwise direction. (b) The time variation of the spatially averaged streamwise velocity.

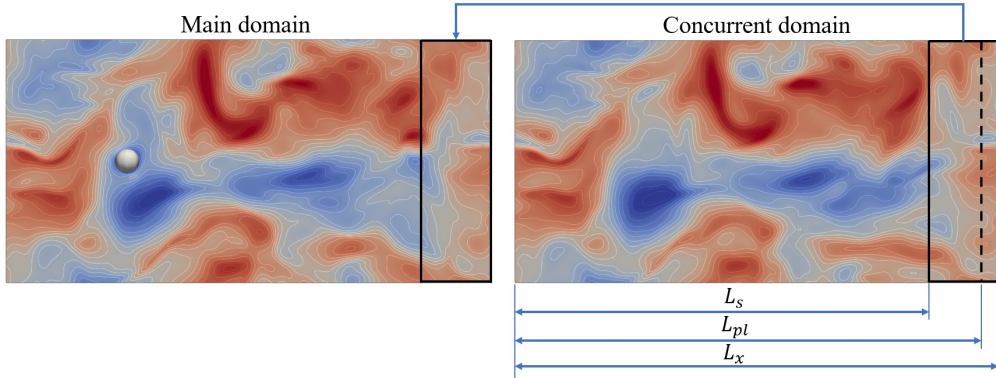


**Figure 3:** Schematic diagram of the concurrent precursor inflow method.

input. Therefore, a forcing method should be employed to maintain the spatially averaged TKE and the turbulence dissipation rate (TDR) to be statistically stationary in the simulation. The main idea behind the turbulent forcing method is to add a forcing term  $f_{TF}$  in the right-hand side of the momentum equation (11), where

$$f_{TF} = A\tilde{\mathbf{u}}^{(2)}. \quad (13)$$

Here  $\tilde{\mathbf{u}}^{(2)}$  represents the large-scale velocity fluctuation obtained by a low-pass filter that preserves the two lowest Fourier modes of the turbulent flow. The time-varying prefactor  $A$  is determined from the TKE balance according to Bassenne, Urzay, Park and Moin (2016)

$$A(t) = \frac{\varepsilon(t) - G[k(t) - k_\infty]/t_{l,\infty}}{2k(t)}, \quad (14)$$

where  $\varepsilon(t) = \langle \nu (\partial u_i / \partial x_j) (\partial u_i / \partial x_j) \rangle$  is the time-varying spatially averaged TDR, the angle bracket  $\langle \cdot \rangle$  denotes spatial averaging,  $k(t) = \langle u'_i u'_i \rangle / 2$  is the time-varying spatially averaged TKE,  $u'_i$  is the flow velocity fluctuation,  $k_\infty$  is the target TKE, and  $G/t_{l,\infty}$  is set to a constant of 50, which can ensure a fast development of background turbulence to a statistically stationary state. Figure 1 shows the time variations of  $k(t)$  and  $\varepsilon(t)$  of a turbulent flow using the turbulence forcing method at  $Re_\lambda = 82$ . It is seen that both  $k(t)$  and  $\varepsilon(t)$  reach a statistically stationary state very quickly once the turbulent forcing is applied.

### 2.3. Removing the influence of particle wake

To calculate the fluid force of a particle in a turbulent environment, it is necessary to superimpose a mean flow on the turbulence to ensure the statistical steady state. If traditional inlet and outlet boundary conditions are applied in the

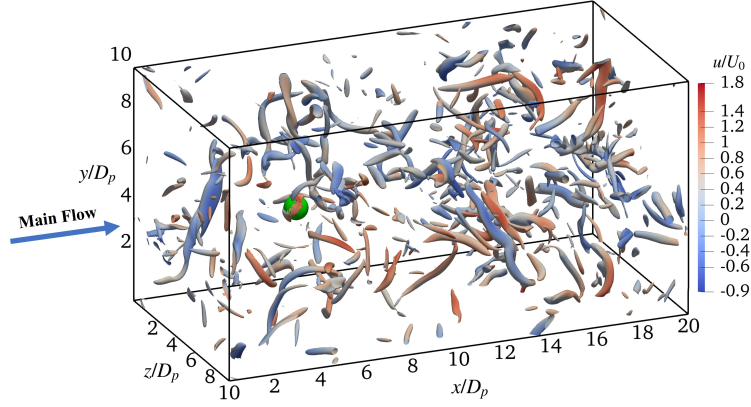


Figure 4: Sketch of the simulation domain.

streamwise direction, the turbulent flow will decay along the streamwise direction, leading to a nonuniform turbulent flow field around the particle. To address this issue, we employ periodic boundary conditions in the streamwise direction. However, the limited extent of the computational domain will inevitably lead to a reduction in the upstream flow velocity experienced by the particle due to the particle wake. Figure 2 illustrates that the mean streamwise flow velocity at the inlet is below  $U_0$  (where  $U_0$  is the desired mean inflow velocity), and the mean streamwise flow velocity all over the domain decreases over time if the influence of the particle wake is not adequately removed.

This work employs a concurrent precursor method, as proposed by [Stevens, Graham and Meneveau \(2014\)](#), to eliminate the impact of particle wake on the upstream flow of the particle, similar to its wide applications in wind turbine/farm flow simulations. We note that both flows are bluff-body flows, and wakes are generated after the obstacles; therefore, the concurrent precursor method can be quite useful in their simulations. This method involves simultaneously simulating a separate flow field with the same configuration free of a particle alongside the flow field that includes a particle, as illustrated in figure 3. At each time step, the flow velocity of the last  $0.09L_x$  ( $L_x$  is the streamwise length of the simulation domain) of the concurrent precursor simulation domain in the streamwise direction is interpolated into the last  $0.09L_x$  of the main simulation domain using the interpolation function as follows:

$$\mathbf{u}_m = w(x) \cdot \mathbf{u}_c + (1 - w(x)) \cdot \mathbf{u}_m, \quad (15)$$

$$w(x) = \begin{cases} \frac{1}{2} \left[ 1 - \cos \left( \pi \frac{x - L_s}{L_{pl} - L_s} \right) \right], & L_s < x \leq L_{pl}, \\ 1, & L_{pl} < x \leq L_x, \end{cases} \quad (16)$$

where  $\mathbf{u}_m$  and  $\mathbf{u}_c$  are the flow velocities in the last  $0.09L_x$  ( $x > 0.91L_x$ ) of the main and concurrent precursor domains, respectively.  $w(x)$  is the interpolation function, with  $L_s = 0.91L_x$  and  $L_{pl} = L_s + 0.75(L_x - L_s) = 0.9775L_x$ , in which  $x$  is the streamwise coordinate. Figure 2 shows that the mean streamwise velocity at the inlet is the desired  $U_0$  and the mean bulk streamwise velocity remains constant over time once the influence of the particle wake is removed by the concurrent precursor simulation method. The influence of the concurrent precursor method on the prediction accuracy of particle drag in uniform flows is evaluated in the Appendix 5.

## 2.4. Simulation setup

The simulation domain in this work spans  $L_x \times L_y \times L_z = 20D_p \times 10D_p \times 10D_p$  ( $D_p$  represents particle diameter) in the  $x$  (streamwise),  $y$  (vertical), and  $z$  (spanwise) directions, respectively, as seen in figure 4. The size of the simulation domain is close to the suggestion of [Elmestikawy, Chéron and van Wachem \(2025\)](#). The periodic boundary conditions are applied in all three directions for the fluid. The finite-size spherical particle is fixed at  $\mathbf{x}_p = (5D_p, 5D_p, 5D_p)$ , namely in the center of the cross-plane and  $5D_p$  from the inlet.

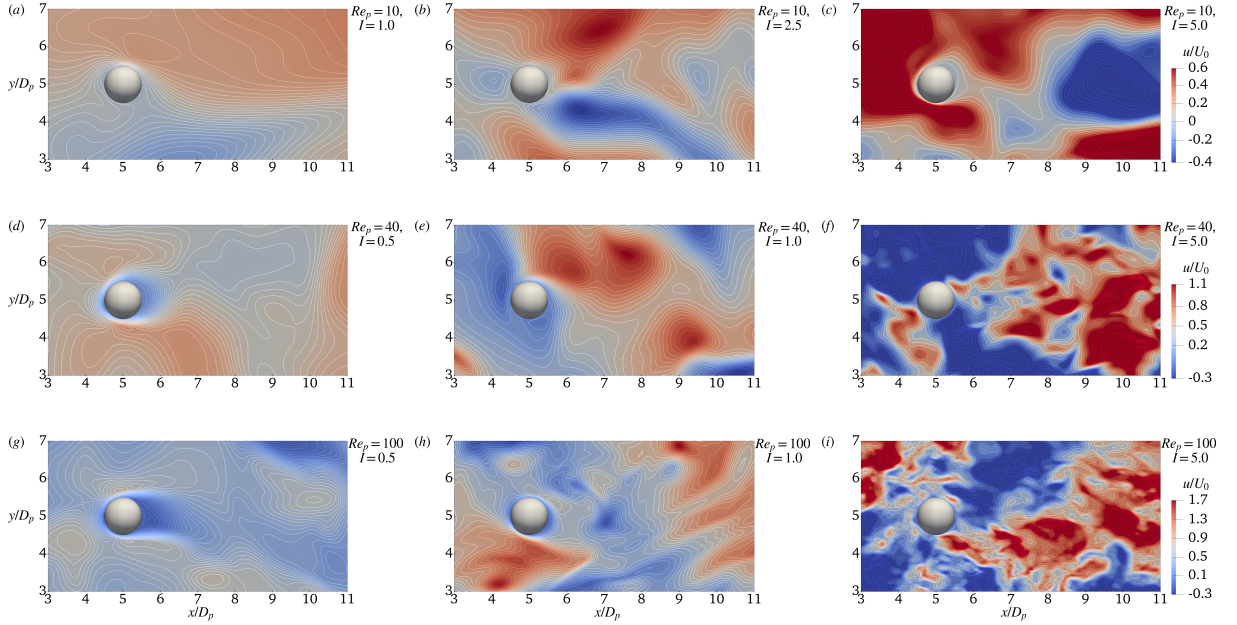


**Figure 5:** Streamwise velocity contours of the flow field around the particle under different conditions.

The kinematic simulation method (Kraichnan, 1970; Saad, Cline, Stoll and Sutherland, 2017) is used to generate the initial velocity field. Then, the turbulent forcing and concurrent precursor inflow methods previously introduced are adopted to maintain statistically stationary turbulence and eliminate the influence of particle wake, respectively. We employ a uniform mesh in all three dimensions to fulfill the prerequisites of the direct-forcing immersed boundary method (Uhlmann, 2005; Breugem, 2012). Moreover, to accurately resolve the smallest turbulent motions within the flow field, the grid size  $h$  must meet the criteria  $h/\eta < 2.1$  (Pope, 2000). Consequently, a grid size of  $h = 0.05$  or  $h = 0.025$  is selected depending on the Kolmogorov scale of turbulence. Meanwhile, the ratio of particle size to grid size  $D_p/h$  ( $D_p = 1$ ) is 20 or 40 in this work, which can sufficiently resolve the flow around the particle.

There are five independent dimensional parameters involved in this problem, *i.e.* the mean inflow velocity (mean slip velocity between particle and flow)  $U_0$ , the particle diameter  $D_p$ , the fluid kinematic viscosity  $\nu$ , the turbulent velocity intensity  $u_{rms}$ , and the mean turbulence dissipation rate  $\varepsilon$ . These parameters can constitute a group of three independent dimensionless variables, like the slip-velocity-based particle Reynolds number  $Re_p = U_0 D_p / \nu$ , the turbulence intensity ratio  $I = u_{rms} / U_0$ , and the particle-to-turbulence scale ratio  $D_p / \eta$ , or the turbulence-velocity-based particle Reynolds number  $Re'_p = u_{rms} D_p / \nu$ ,  $I = u_{rms} / U_0$ , and  $D_p / \eta$ , or the Taylor-scale-based turbulence Reynolds number  $Re_\lambda = u_{rms} \lambda / \nu$ ,  $I = u_{rms} / U_0$ , and  $D_p / \eta$ , where the Kolmogorov-scale size  $\eta = (\nu^3 / \varepsilon)^{1/4}$  and the Taylor-microscale size  $\lambda = (15 \nu u_{rms}^2 / \varepsilon)^{1/2}$ . Different combinations of the dimensionless parameters are, in fact, equivalent to one another, *e.g.*  $Re'_p = I Re_p$ ,  $Re_\lambda = \sqrt{15} (D_p / \eta)^{-2} Re_p^2$ . There are totally 28 cases in the PRDNS, covering  $Re_p = 1 \sim 300$ ,  $D_p / \eta = 1.6 \sim 76.9$ , and  $I = 0.1 \sim 20$ . Table 4 in the Appendix 5 shows the corresponding values of the parameters in the PRDNS in the upper part of  $D_p / \eta$  greater than 1. Furthermore, to cover a larger range of  $D_p / \eta$ , point-particle direct numerical simulation (PPDNS) using the Schiller-Neumann (S-N) drag law (Schiller and Naumann, 1933) is also conducted with 15 cases, covering  $Re_p = 0.1 \sim 3.2$ ,  $D_p / \eta = 0.22 \sim 0.99$ , and  $I = 0.5 \sim 20$ , as shown in the bottom part of table 4 in the Appendix 5.

## 2.5. Flow characteristics

Figure 5 illustrates the streamwise velocity contours of the flow field around the particle under different conditions. In general, the particle is fully immersed in the turbulence, and a very thin boundary layer can be observed adjacent to the particle. The particle may interact with and modify the local flow, although only one particle is considered and the disperse phase is quite dilute. The modulation effect of the finite-size particle on the evolution of the turbulence is left for future studies. Furthermore, it can be seen that as the turbulence intensity progressively increases, the flow structures



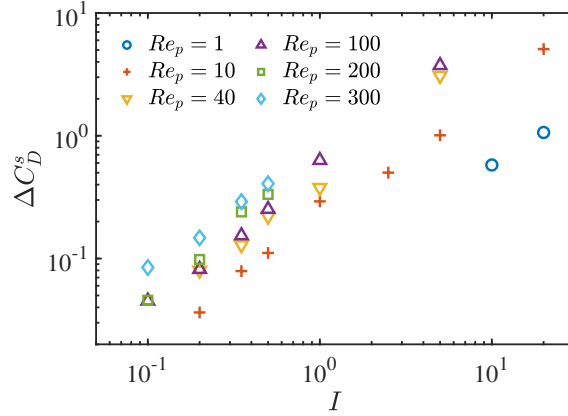


**Figure 6:** Relative increments of the mean particle drag coefficient at different turbulent intensities and particle Reynolds numbers.

surrounding the particles become more complex and multiscale due to the increase in the flow Reynolds number, and the magnitude of the flow velocity gradually intensifies. Furthermore, comparing the second row ( $Re_p = 40$ ) with the third row ( $Re_p = 100$ ), it is evident that an increase in the particle Reynolds number leads to a greater abundance of small-scale structures within the flow field, which can also be attributed to the increase of the flow Reynolds number with the same turbulence intensity ratio  $I$  (see table 4).

### 3. Fluid force models

#### 3.1. Mean drag force model

This section presents new correlations for the mean particle drag coefficient that consider turbulence effects. For each condition shown in table 4 of Appendix 5, a time series of fluid force can be calculated from PRDNS or PPDNS. The drag force is the part that aligns with the mean slip velocity direction, which is the direction in the mean flow. Figure 6 illustrates the relative increments of the mean particle drag coefficient across various turbulence intensities and particle Reynolds numbers, showing only the PRDNS data. The relative increments in the mean particle drag coefficient are always positive, suggesting that turbulence enhances the particle drag force compared to the uniform flow condition. The relative increase  $\Delta C_D$  also increases with the turbulence intensity ratio  $I$  with the same particle Reynolds number. These observations are consistent with previous studies (Brucato et al., 1998; Zeng et al., 2008; Homann et al., 2013; Wang et al., 2023; Peng and Wang, 2023; Xia et al., 2022, 2023).

The correlation (4) proposed by Homann et al. (2013) for the mean particle drag coefficient in turbulence was based on the following two assumptions: (1) The instantaneous particle drag is determined by the S-N drag law using the instantaneous slip velocity; (2) the instantaneous slip velocity follows a Gaussian distribution. With similar assumptions, Xia et al. (2022) proposed the correlation (8). In the following, we briefly present the general derivation of the correlations (4) and (8). Commencing with the instantaneous slip velocity  $\mathbf{U}_s = (U_s, V_s, W_s)$ , the instantaneous particle drag force can be written as

$$F_D(t) = \frac{24}{\tilde{Re}_p(t)} \left[ 1 + 0.15 \tilde{Re}_p^{0.687}(t) \right] \cdot \frac{1}{2} \rho_f |\mathbf{U}_s(t)| U_s(t) A, \quad (17)$$

where  $\tilde{Re}_p(t) = |\mathbf{U}_s(t)| D_p / \nu$  is the particle Reynolds number based on the instantaneous slip velocity,  $\rho_f$  is the fluid density, and  $A = \pi D_p^2 / 4$  is the particle sectional area.

Therefore, the mean particle drag coefficient can be obtained as follows:

$$C_D = \frac{\overline{F_D(t)}}{(1/2) \rho_f \overline{U_s^2} A} = \frac{24}{Re_p} \frac{\overline{U_s(t) \left[ 1 + 0.15 \tilde{Re}_p^{0.687}(t) \right]}}{\overline{U_s}}$$



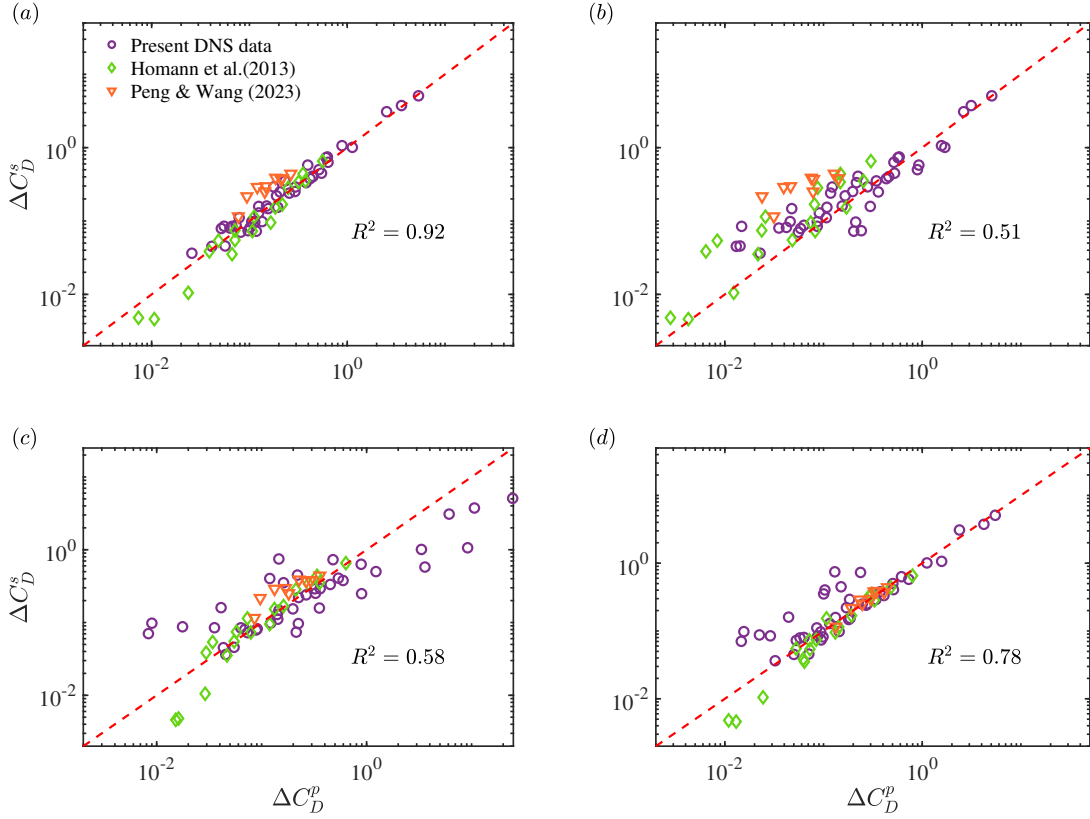


**Figure 7:** Comparisons of the relative increment of the mean particle drag coefficient between the PRDNS data and the predictions by (a) the correlation (21), (b) the correlation (20), (c) the correlation (3), and (d) the correlation (5). Here,  $R^2$  represents the coefficient of determination; the closer  $R^2$  is to one, the better the agreement between the prediction and the DNS data.

$$\begin{aligned}
 &= \frac{24}{Re_p} \left[ 1 + \frac{\overline{0.15 \tilde{Re}_p^{0.687}(t) U_s(t)}}{\bar{U}_s} \right] \\
 &= \frac{24}{Re_p} \left( 1 + 0.15 Re_p^{0.687} f_1 \right), \tag{18}
 \end{aligned}$$

where  $Re_p = \bar{U}_s D_p / \nu$  ( $\bar{U}_s = U_0$  is the mean slip velocity) and

$$f_1 = \overline{|U_s(t)|^{0.687} U_s(t)} / \bar{U}_s^{1.687}. \tag{19}$$

Therefore,

$$\Delta C_D = \frac{0.15 Re_p^{0.687}}{1 + 0.15 Re_p^{0.687}} (f_1 - 1).$$

To close (19), although it can be assumed that the slip velocity  $U_s$  follows a Gaussian distribution with a mean of  $(\bar{U}_s, 0, 0)$  and a standard variation of  $(u_{rms}, u_{rms}, u_{rms})$ , it is very difficult to get an explicit expression of  $f_1$  (Homann et al., 2013). Therefore, the numerical approach is usually used. For example, Xia et al. (2022) employed numerical integration to calculate the increase in mean drag as a function of  $I$ . Here we stochastically generate the  $U_s$  data and

determine the relationship between  $f_1$  and  $I$ , *i.e.*  $f_1 = 1 + 0.815I^{1.687}$  when  $I \leq 1$  and  $f_1 = 1.662I^{0.687}$  when  $I > 1$ . Consequently, the relative increment of the mean particle drag coefficient can be modeled as follows:

$$\Delta C_D = \begin{cases} \frac{0.122 Re_p^{0.687}}{1 + 0.15 Re_p^{0.687}} I^{1.687}, & I \leq 1 \\ \frac{0.15 Re_p^{0.687}}{1 + 0.15 Re_p^{0.687}} (1.662 I^{0.687} - 1), & I > 1. \end{cases} \quad (20)$$

In the derivation of the correlation (20),  $f_1$  is assumed to be a function of  $I$  only, as it depends only on  $U_s$ . However, [Homann et al. \(2013\)](#) found that their correlation (4) does not match the PRDNS data very well at high  $I$ , so they proposed (3) by introducing the flow Reynolds number as an additional parameter. This is because the physical problem is controlled by three independent dimensionless parameters, while only two are invoked in (20). Following a similar idea, we introduce the Taylor-microscale-based Reynolds number  $Re_\lambda$  in the modeling  $f_1$ . Therefore, the second correlation is obtained by fitting the present PRDNS data with a form of  $f_1 = aI^b Re_\lambda^c + d$ , which is

$$\Delta C_D = \frac{0.015 Re_p^{0.687}}{1 + 0.15 Re_p^{0.687}} I^{0.858} Re_\lambda^{0.474}. \quad (21)$$

The fitting is performed with the curve fitting toolbox of MATLAB by prescribing the functional form. The correlations (21) and (20) are compared to the PRDNS data of the present study, [Homann et al. \(2013\)](#) and [Peng and Wang \(2023\)](#) in figure 7, as well as the correlations (3) and (5). The correlation (21) exhibits the best concordance with the PRDNS data. It is also noted that  $\Delta C_D \rightarrow 0$  as  $I \rightarrow 0$  or  $Re_\lambda \rightarrow 0$ , which means that the mean particle drag force precisely adheres to the S-N drag law with a negligible turbulence effect.

### 3.2. Fluctuating drag force model

In this section, a stochastic model based on the Langevin equation is proposed for the fluctuating particle drag force. The fluctuating drag force denotes the component of the drag force obtained by subtracting its mean value, *i.e.*  $F'_D = F_D - \bar{F}_D$ . The fluctuating particle drag force in turbulence is intrinsically connected with turbulence fluctuations; hence,  $u_{rms}^2$  is utilized as the reference velocity for normalizing the fluctuating particle drag force, which is

$$C'_D = \frac{F'_D}{(1/2)\rho_f u_{rms}^2 A}. \quad (22)$$

Figure 8 shows the probability distribution function (PDF) of the fluctuating particle drag coefficient. The  $R^2(C'_D)$  in table 4 of the Appendix 5 presents the coefficient of determination between the PDF of the fluctuating drag coefficient and the Gaussian distribution, where the mean and variance of the Gaussian distribution are derived from the PRDNS data. It can be seen that the fluctuating particle drag coefficient follows the Gaussian distribution very well under different conditions. A stationary Gaussian process is completely characterized by its mean, variance, and autocorrelation function. Originally proposed as a stochastic model for the velocity of a microscopic particle undergoing Brownian motion, the Langevin equation ([Langevin, 1908](#)) can yield a Gaussian distribution of the particle velocity ([Pope, 2000](#)). Therefore, the Langevin equation can be reasonably adopted to model the temporal variation of the fluctuating particle drag coefficient as follows:

$$dC'_D(t) = -\frac{C'_D(t)}{T_D} dt + C'_{D,rms} \sqrt{\frac{2}{T_D}} dW, \quad (23)$$

where  $C'_{D,rms}$  and  $T_D$  represent the RMS value and integral time scale of the fluctuating particle drag coefficient, respectively, which require modeling.  $dW$  is the discrete Wiener process, and  $dt$  is the time step. We note that the Langevin equation is not the only option to model a Gaussian process, but we adopt it because of its simplicity and wide applications.

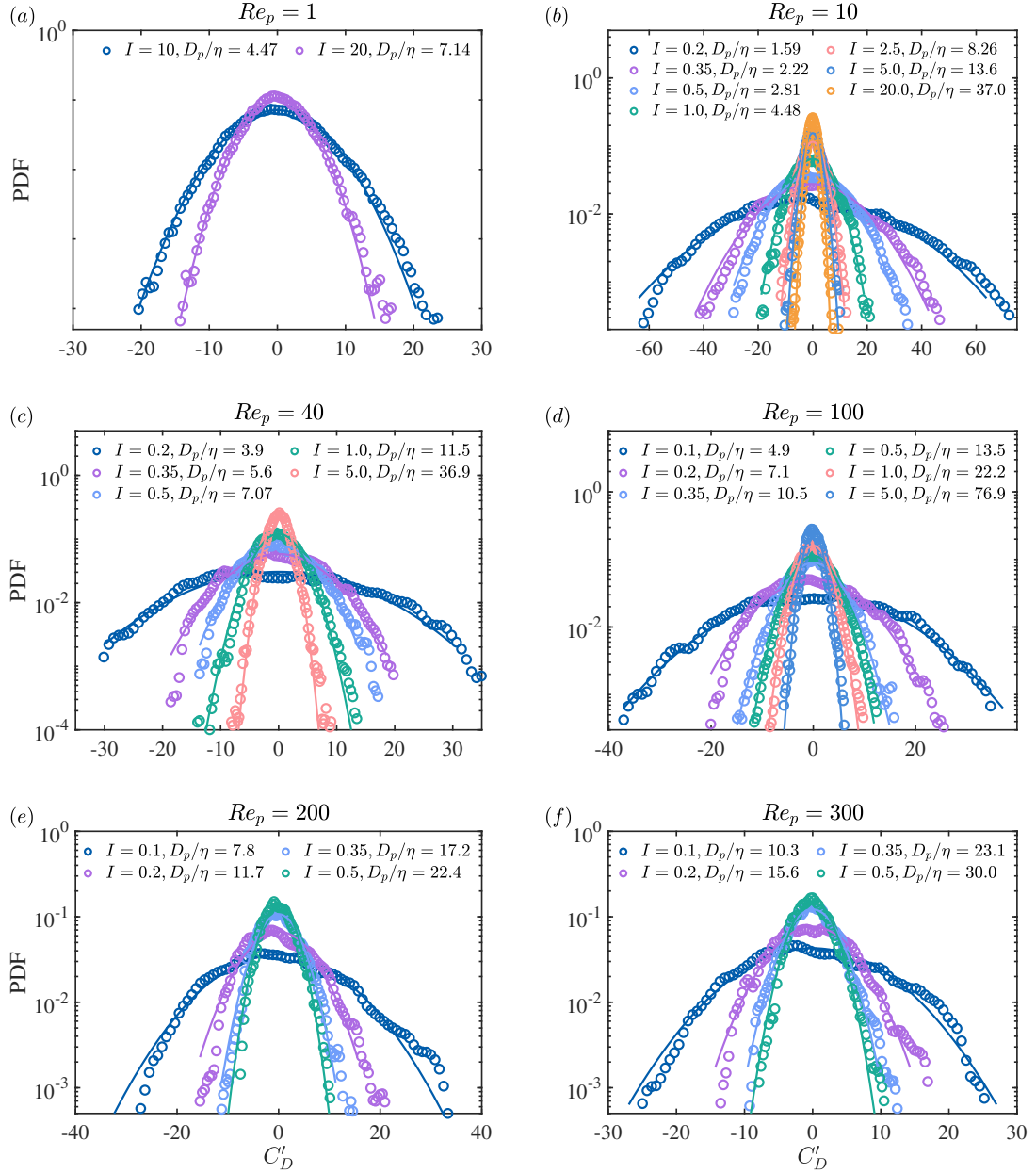


**Figure 8:** The probability distribution functions of the fluctuating particle drag coefficient. The symbols are the PRDNS data, and the solid lines are Gaussian distributions.

### 3.2.1. Modeling particle drag fluctuation intensity

First, assuming that the instantaneous particle drag force follows the S-N drag law and that the slip velocity follows a Gaussian distribution, we employ a similar derivation for the correlation (20) to model  $C'_{D,rms}$  as

$$\begin{aligned}
 C'_{D,rms} &= \text{RMS}(C'_D(t)) = \text{RMS}(C_D(t)) \\
 &= \frac{24\nu}{u_{rms} D_p} \text{RMS} \left[ \frac{U_s(t) \left( 1 + 0.15 \tilde{Re}_p^{0.687}(t) \right)}{u_{rms}} \right]
 \end{aligned}$$

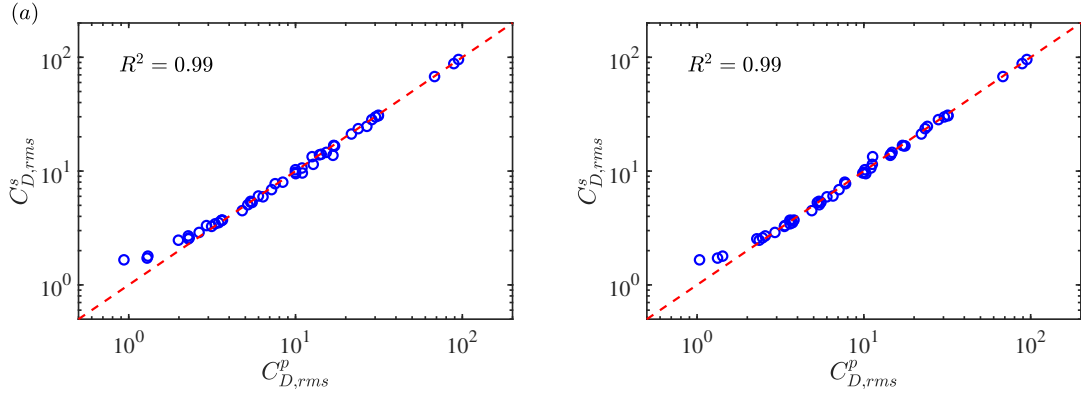


**Figure 9:** Comparison of the particle drag fluctuation intensities predicted by (a) the correlation (26) and (b) the correlation (27) with the DNS data.

$$\begin{aligned}
 &= \frac{24\nu}{u_{rms}D_p} \left[ 1 + \text{RMS} \left( \frac{0.15 \tilde{Re}_p^{0.687}(t) U_s(t)}{u_{rms}} \right) \right] \\
 &= \frac{24\nu}{u_{rms}D_p} \left[ 1 + 0.15 \left( \frac{u_{rms}D_p}{\nu} \right)^{0.687} \text{RMS} \left( \frac{|U_s(t)|^{0.687} U_s(t)}{u_{rms}^{1.687}} \right) \right] \\
 &= \frac{24}{Re'_p} \left( 1 + 0.15 Re_p'^{0.687} f_2 \right), \tag{24}
 \end{aligned}$$

where  $Re'_p = u_{rms}D_p/\nu$  is the turbulence-velocity-based particle Reynolds number,  $\text{RMS}(\cdot)$  represents the computation of RMS and the function we need to close (24) is

$$f_2 = \text{RMS} \left( \frac{|U_s(t)|^{0.687} U_s(t)}{u_{rms}^{1.687}} \right). \tag{25}$$

Similar to  $f_1$  in (19), it is very difficult to obtain an explicit expression for  $f_2$ . Therefore, the numerical method used for  $f_1$  is also employed to determine  $f_2$ .

$$C'_{D,rms} = \begin{cases} \frac{24}{Re'_p} \left( 1 + 0.253 Re_p'^{0.687} \right), & I \leq 0.5, \\ \frac{24}{Re'_p} \left[ 1 + 0.15 Re_p'^{0.687} (1.702 + 0.347 I^{-1.687}) \right], & I > 0.5. \end{cases} \tag{26}$$

On the other hand, only two of the three independent dimensionless parameters are included in the correlation (26). In turn,  $f_2$  is determined by fitting the PRDNS and PPDNS data while accounting for an entire set of three dimensionless parameters for establishing the second correlation for particle drag fluctuation intensity, which is

$$C'_{D,rms} = \frac{24}{Re'_p} \left[ 1 + 0.15 Re_p'^{0.687} \left( 1.702 + 0.556 I^{-0.891} \left( \frac{D_p}{\eta} \right)^{0.111} \right) \right]. \tag{27}$$

Figure 9 compares the predicted particle drag fluctuation intensities calculated from correlations (26) and (27) against the PRDNS and PPDNS data. Both correlations exhibit excellent agreement with the PRDNS data. In addition, it is observed that  $F'_{D,rms} \rightarrow 0$  when  $I \rightarrow 0$ , thus, the singularity of  $C'_{D,rms}$  in the correlation (27) can be avoided in terms of  $F'_{D,rms}$ .

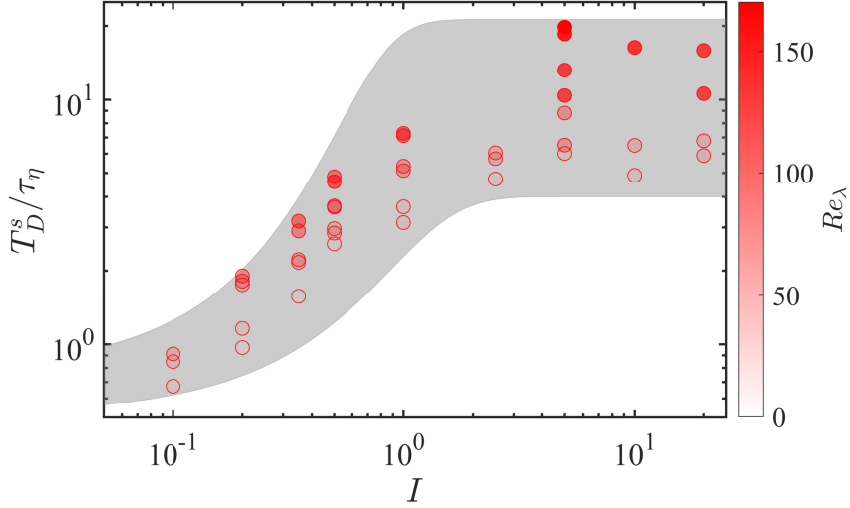


**Figure 10:** Relationship between the particle drag time scale ratio and the turbulence intensity ratio.

### 3.2.2. Modeling particle drag fluctuation time scale

The time scale  $T_D$  involved in equation (23) is the integral time scale of the fluctuating particle drag coefficient, which is defined by

$$T_D = \int_0^{\infty} R_{C'_D C'_D}(\tau) d\tau, \quad (28)$$

in which  $R_{C'_D C'_D}(\tau) = \langle C'_D(t) C'_D(t + \tau) \rangle / \langle C'_D(t)^2 \rangle$  is the autocorrelation of the fluctuating particle drag coefficient. If  $T_D$  is normalized by  $\tau_\eta$  ( $\tau_\eta = (\nu/\varepsilon)^{1/2}$  is the Kolmogorov time scale.), it can be assumed to be fully determined by three independent dimensionless parameters, such as

$$\frac{T_D}{\tau_\eta} = f_3(Re_p, I, D_p/\eta). \quad (29)$$

It is usually natural to use power products to model  $f_3$  (Homann et al., 2013; Xia et al., 2022; Peng and Wang, 2023), *i.e.*

$$\frac{T_D}{\tau_\eta} = a I^b Re_p^c (D_p/\eta)^d. \quad (30)$$

By taking the logarithm of both sides of equation (30), the values of the unknown parameters  $a, b, c$  and  $d$  can be determined by fitting the PRDNS and PPDNS data via a multidimensional linear regression, which yields

$$\frac{T_D}{\tau_\eta} = 1.175 I^{1.415} Re_p^{1.074} (D_p/\eta)^{-1.132}. \quad (31)$$

Upon a thorough examination of the PRDNS and PPDNS data, we observed a robust correlation between the time scale ratio  $T_D/\tau_\eta$ , the Taylor-microscale-based Reynolds number  $Re_\lambda$ , and the turbulence intensity ratio  $I$ . This is reasonable since the fluctuation of the particle drag should probably correlate with the turbulence properties. The time scale ratio  $T_D/\tau_\eta$  is observed to increase with  $Re_\lambda$ . Simultaneously, we find that the time scale ratios exhibit relative similarity at high turbulence intensities with comparable  $Re_\lambda$ , indicating a potential convergence towards an asymptotic value at high  $I$ , as shown in figure 10. Therefore, we propose another form for modeling the time scale ratio according to the above observations, as

$$\frac{T_D}{\tau_\eta} = \frac{a Re_\lambda^b}{1 + c e^{-dI}}. \quad (32)$$

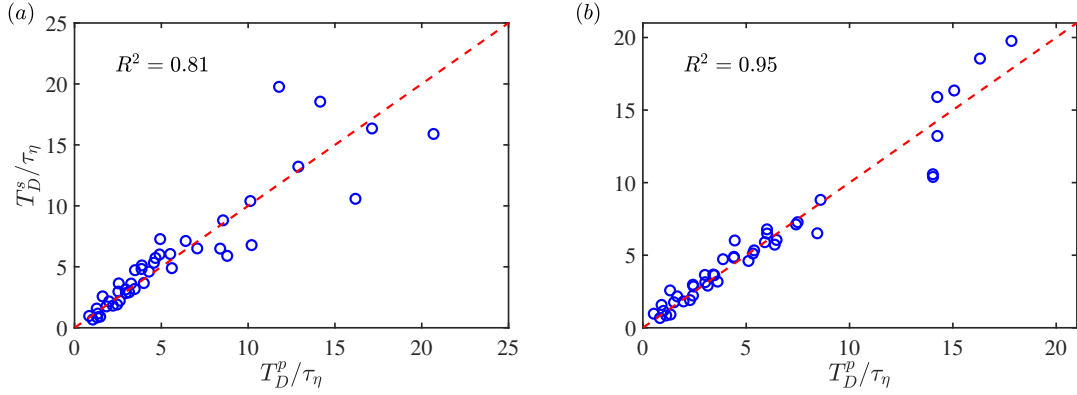


**Figure 11:** Comparison of the time scale ratio of the fluctuating particle drag coefficient predicted by (a) the correlation (31) and (b) the correlation (33) with the DNS data.

By fitting the PRDNS data, the second correlation for the time scale is obtained, which is

$$\frac{T_D}{\tau_\eta} = \frac{0.634 Re_\lambda^{0.654}}{1 + 4.614 e^{-2.282I}}. \quad (33)$$

Figure 11 (a) compares the time scale of the fluctuation of particle drag between the DNS data and the correlation (31). The prediction of the correlation (31) is found to not agree well with the DNS data. Figure 11 (b) shows the comparison of the time scale ratio  $T_D/\eta$  from the DNS data and the correlation (33). We can see that the prediction of the correlation (33) is much more accurate than the correlation (31).

### 3.3. Lateral force model

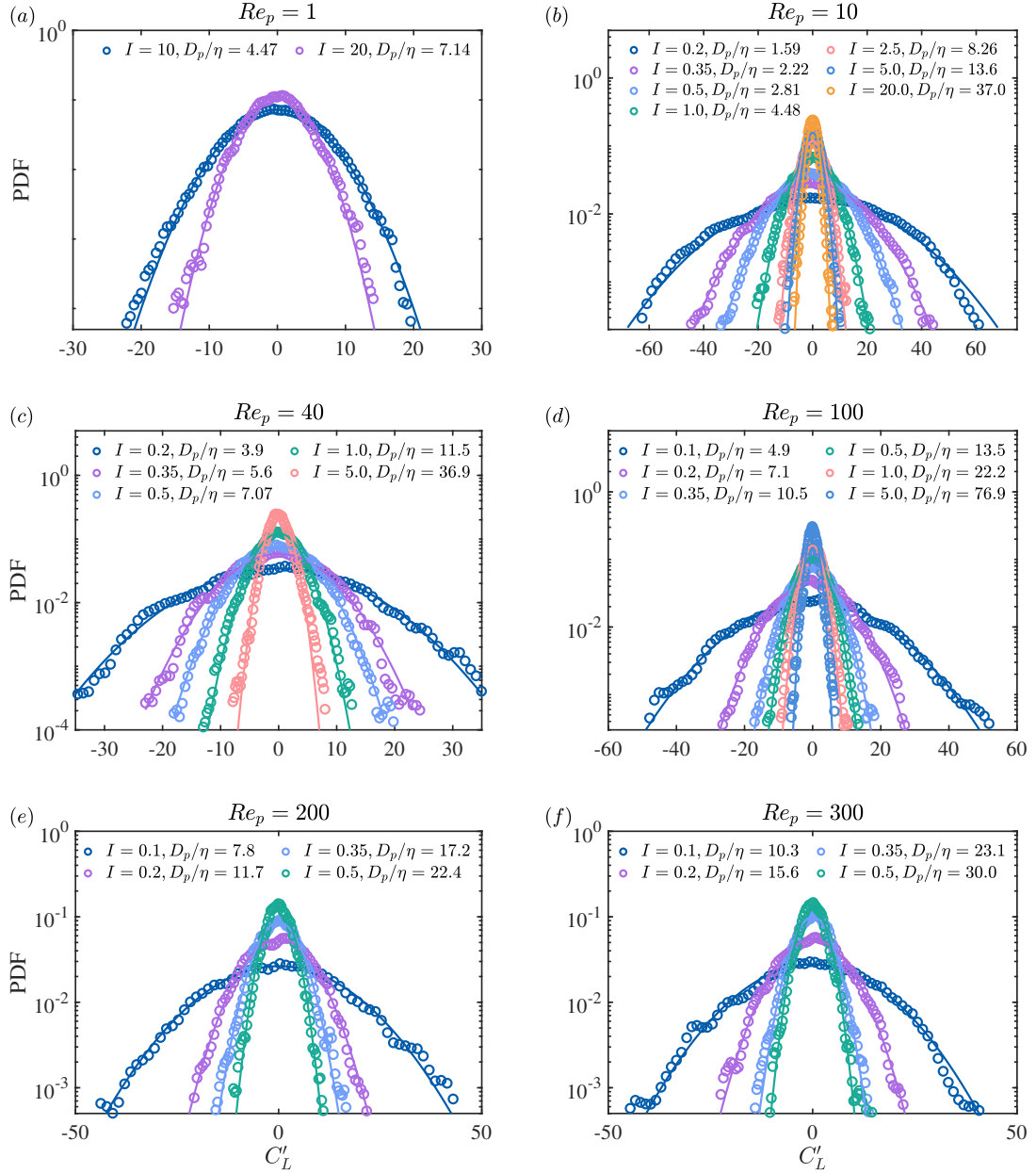
In this section, we propose a stochastic model for the instantaneous lateral fluid force based on the Langevin equation, similar to the fluctuating drag force. The three components of the fluid force that act on the particle include the lateral forces, which are the components perpendicular to the mean direction of the slip velocity. When the incoming flow is uniform at  $Re_p < 210$ , the mean lift of the particle is zero due to the axisymmetric nature of the particle wake. In contrast, the mean lift is not zero due to the emergence of an asymmetric particle wake when  $Re_p > 210$ ; for example, the mean lift coefficient is around 0.06 when  $Re_p = 300$  (Johnson and Patel, 1999; Kim, Kim and Choi, 2001; Ploumhans, Winkelmann, Salmon, Leonard and Warren, 2002; Kim and Choi, 2002; Constantinescu and Squires, 2003; Niazmand and Renksizbulut, 2003; Wang and Zhang, 2011; Liska and Colonius, 2017). Moreover, given uniform inflow conditions, the mean particle lift is approximately two orders of magnitude less than the mean particle drag. In turbulent inflow, we found that the mean lateral force on the particle at  $Re_p = 300$  is significantly less than that in uniform flow at the same particle Reynolds number. This may be due to turbulence disrupting the asymmetry of particle wakes, rendering them more symmetric in a statistical sense. Therefore, we assume that the mean particle lateral force is roughly zero and focus solely on modeling the fluctuating component of the particle lateral force.

Figure 12 shows the probability distribution functions of the fluctuating lateral force coefficient of the particle. The  $R^2(C'_L)$  in table 4 of the Appendix 5 represents the coefficient of determination between the PDF of the fluctuating lateral force coefficient and the Gaussian distribution, where the mean and variance of the Gaussian distribution are derived from the PRDNS data. It can be seen that it can be well approximated by the Gaussian distribution, similar to the fluctuating drag force. Consequently, the stochastic Langevin equation is also used to model the fluctuating particle lateral force as follows:

$$dC_L(t) = -\frac{C_L(t)}{T_L} dt + C_{L,rms} \sqrt{\frac{2}{T_L}} dW, \quad (34)$$

where  $C_L(t)$  is the instantaneous particle lateral force coefficient with a zero mean, and  $C_{L,rms}$  and  $T_L$  are the RMS and integral time scale of the fluctuating lateral force coefficient, respectively.





**Figure 12:** The probability distribution functions of the fluctuating particle lateral force coefficient. The symbols are the PRDNS data, and the solid lines are Gaussian distributions.

### 3.3.1. Modeling particle lateral force fluctuation intensity

The lateral force is perpendicular to the mean slip velocity. Therefore, the instantaneous particle lateral force can be written as

$$F_L(t) = \frac{24}{\tilde{Re}_p(t)} \left[ 1 + 0.15 \tilde{Re}_p^{0.687}(t) \right] \cdot \frac{1}{2} \rho_f |\mathbf{U}_s(t)| V_s(t) A, \quad (35)$$

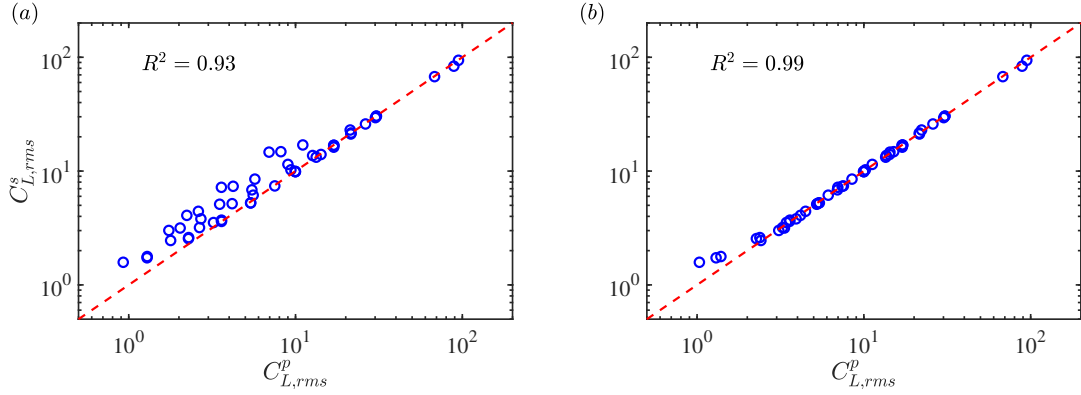


**Figure 13:** Comparison of the particle lateral force fluctuation intensities predicted by (a) the correlation (39) and (b) the correlation (40).

in which  $V_s(t)$  is the instantaneous lateral slip velocity. So, the instantaneous lateral force coefficient can be expressed as

$$\begin{aligned} C_L(t) &= \frac{F_L(t)}{(1/2)\rho_f u_{rms}^2 A} \\ &= \frac{24\nu}{u_{rms} D_p} \frac{V_s(t)}{u_{rms}} \left[ 1 + 0.15 \tilde{Re}_p(t)^{0.687} \right]. \end{aligned} \quad (36)$$

As a result,  $C_{L,rms}$  can be calculated by

$$\begin{aligned} C_{L,rms} &= \text{RMS}(C_L(t)) \\ &= \frac{24\nu}{u_{rms} D_p} \text{RMS} \left[ \frac{V_s(t) (1 + 0.15 \tilde{Re}_p(t)^{0.687})}{u_{rms}} \right] \\ &= \frac{24\nu}{u_{rms} D_p} \left[ 1 + \text{RMS} \left( \frac{0.15 \tilde{Re}_p(t)^{0.687} V_s(t)}{u_{rms}} \right) \right] \\ &= \frac{24\nu}{u_{rms} D_p} \left[ 1 + 0.15 \left( \frac{u_{rms} D_p}{\nu} \right)^{0.687} \text{RMS} \left( \frac{|U_s(t)|^{0.687} V_s(t)}{u_{rms}^{1.687}} \right) \right] \\ &= \frac{24}{Re'_p} \left( 1 + 0.15 Re_p'^{0.687} f_4 \right), \end{aligned} \quad (37)$$

where

$$f_4 = \text{RMS} \left( \frac{|U_s(t)|^{0.687} V_s(t)}{u_{rms}^{1.687}} \right). \quad (38)$$

Similar to  $f_1$  in (19) and  $f_2$  in (25), the numerical method is used to determine  $f_4$ , which yields

$$C_{L,rms} = \begin{cases} \frac{24}{Re'_p} \left( 1 + 0.15 Re_p'^{0.687} + 0.162 Re_p'^{0.687} I^{1.131} \right), & I \leq 0.5 \\ \frac{24}{Re'_p} \left[ 1 + 0.15 Re_p'^{0.687} (1.702 + 0.11 I^{-1.875}) \right], & I > 0.5. \end{cases} \quad (39)$$

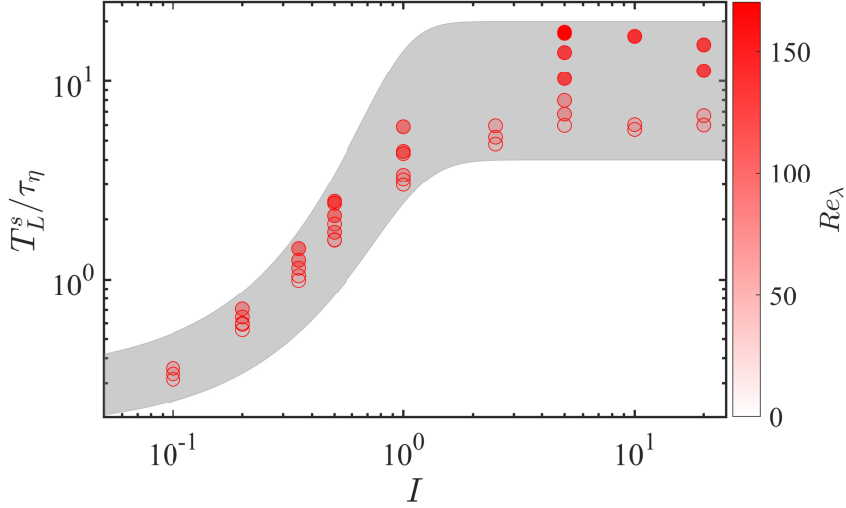


**Figure 14:** Relationship between the particle lateral force time scale ratio and the turbulence intensity ratio.

On the other hand, as in the correlation (27), we introduce the complete three independent dimensionless parameters to determine  $f_4$ . The fitting expression is as follows:

$$C_{L,rms} = \frac{24}{Re'_p} \left[ 1 + 0.15 Re'_p{}^{0.687} \left( 1.689 + 0.226 I^{-1.173} \left( \frac{D_p}{\eta} \right)^{0.432} \right) \right]. \quad (40)$$

Figure 13 compares the RMS of the fluctuating particle lateral force coefficient calculated by PRDNS and PPDNS with the correlations (39) and (40). The predictions obtained from the correlation (40) agree more closely with the DNS data. Similarly to the drag fluctuation, it can be found that  $F'_{L,rms} \rightarrow 0$  when  $I \rightarrow 0$ , so the singularity of  $C'_{L,rms}$  in the correlation (27) can be avoided in terms of  $F'_{L,rms}$ .

### 3.3.2. Modeling particle lateral force fluctuation time scale

The time scale  $T_L$  in equation (34) is defined by

$$T_L = \int_0^\infty R_{C_L C_L}(\tau) d\tau, \quad (41)$$

where  $R_{C_L C_L}$  is the autocorrelation of the fluctuating particle lateral force coefficient.

Similar to the model of  $T_D$ , we first assume that the time scale ratio  $T_L/\tau_\eta$  is a power product of the particle Reynolds number  $Re_p$ , turbulence intensity ratio  $I$  and the scale ratio  $D_p/\eta$ , *i.e.*

$$\frac{T_L}{\tau_\eta} = f_5(Re_p, I, D_p/\eta) = a I^b Re_p^c (D_p/\eta)^d. \quad (42)$$

The values of the unknown parameters  $a$ ,  $b$ ,  $c$ , and  $d$  can be determined by fitting the PRDNS and PPDNS data by multidimensional linear regression after applying the logarithm to both sides of (42), resulting in

$$\frac{T_L}{\tau_\eta} = 0.953 I^{1.496} Re_p^{0.946} (D_p/\eta)^{-1.048}. \quad (43)$$

On the other hand, from the PRDNS data, it is found that the time scale ratio  $T_L/\eta$  increases with the turbulence intensity ratio  $I$  and reaches an asymptotic value at high  $I$ , as shown in figure 14. Therefore, another model with the

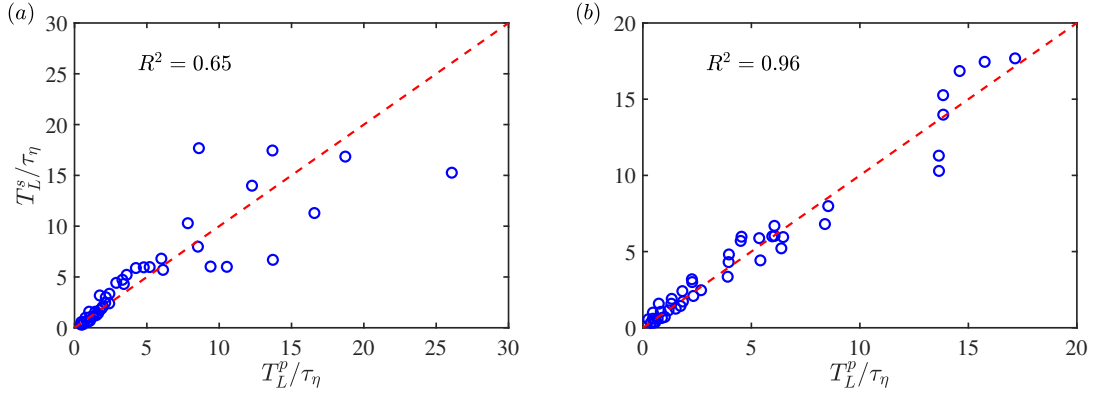


**Figure 15:** Comparison of the particle lateral force fluctuation time scale ratio predicted by (a) the correlation (43) and (b) the correlation (44) with the DNS data.

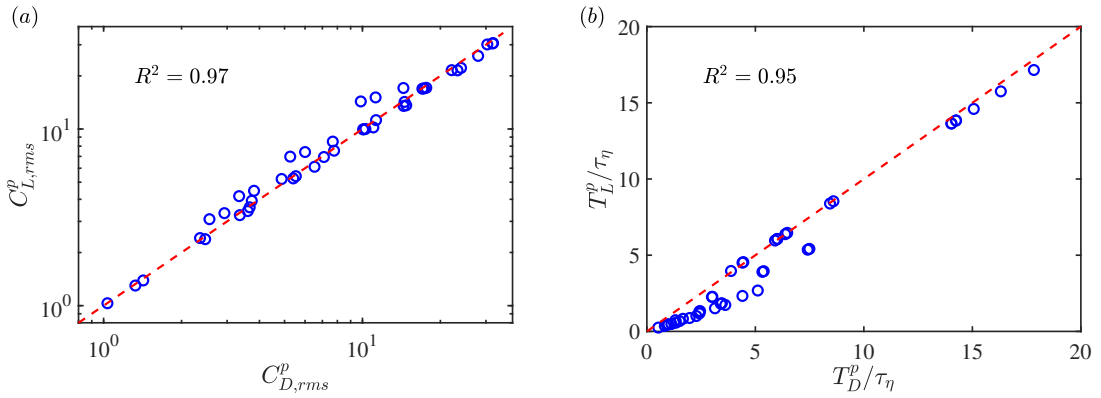


**Figure 16:** Similarities between the fluctuating drag force and lateral force models: (a) fluctuation intensity and (b) time scale.

same form as (32) is obtained as

$$\frac{T_L}{\tau_\eta} = \frac{0.708 Re_\lambda^{0.625}}{1 + 13.012 e^{-2.565I}}. \quad (44)$$

Figure 15 compares the time scale ratio  $T_L/\tau_\eta$  of the PRDNS and PPDNS data with the correlations (43) and (44). The correlation (44) is seen to produce predictions far more accurate than the correlation (43).

The similarities of the fluctuation intensities and time scales predicted by the fluctuating drag force and lateral force models are given in figure 16. It can be seen that the predictions from the two models are quite similar. Therefore, the stochastic model for the fluctuating drag force can be adopted in all directions, which can significantly reduce the complexity of the model implementation. In addition, we note that the fluid force fluctuations in the three directions are statistically independent on the basis of our PRDNS and PPDNS data; hence, they can be calculated separately.

#### 4. Validation of the model

In this section, we will validate our model by simulating the motion of a finite-size particle in a turbulent flow and the dispersion of small particles in a turbulent channel flow to illustrate the prediction capabilities of the model for both finite-size and point particles. The inputs of the model are the mean flow and turbulence quantities, *i.e.* mean flow velocity, TKE and TDR, similar to a point-particle Reynolds-averaged Navier–Stokes (PPRANS) simulation; thus, we

**Table 2**

Parameters of the motion of a finite-size particle in a turbulent flow, where  $Re_{p0} = U_0 D_p / \nu$  is the initial particle Reynolds number.

Case	$Re_{p0}$	$I$	$D_p / \eta$
1	1	2.5	1.8
2	1	5.0	2.8
3	10	0.1	1.1
4	10	0.5	2.8
5	10	5.0	13.3
6	40	5.0	37.0
7	100	1.0	22.2
8	300	0.5	29.6

will refer to it as "PPRANS+SFM", where SFM stands for the stochastic force model. In addition, a point-particle simulation with the S-N drag law is employed to test the turbulence effect, and we refer to it as "PPRANS" in the following. We also conduct DNS simulations to provide the corresponding references in the two problems.

#### 4.1. The motion of a finite-size particle in turbulence

The first problem is with a finite-size particle released and freely moving in a turbulent flow. The background flow is homogeneous and isotropic turbulence superimposed by a streamwise uniform flow, similar to the PRDNS of a fixed particle. The particle diameter is  $D_p$ , and the simulation domain size is  $L_x \times L_y \times L_z = 20D_p \times 10D_p \times 10D_p$ . The periodic boundary condition is used for the flow field and the motion of the particles in the three directions. The initial position of the particle is  $(x_p, y_p, z_p) = (5D_p, 5D_p, 5D_p)$ , the same as in fixed particle cases, and the initial velocity of the particle is 0. Eight cases of different conditions are simulated using PRDNS for validation, as listed in table 2.

For PPRANS+SFM, the equations of particle motion are

$$\frac{d\mathbf{x}_p}{dt} = \mathbf{v}_p, \quad (45)$$

$$\frac{d\mathbf{v}_p}{dt} = (1 + \Delta C_D) \left( 1 + 0.15 Re_p^{0.687} \right) \frac{\mathbf{U} - \mathbf{v}_p}{\tau_p} + \frac{3\rho_f u_{rms}^2}{4\rho_p D_p} \mathbf{C}', \quad (46)$$

$$d\mathbf{C}'(t) = -\frac{\mathbf{C}'(t)}{T_D} dt + C'_{D,rms} \sqrt{\frac{2}{T_D}} d\mathbf{W}, \quad (47)$$

in which,

$$\Delta C_D = \frac{0.015 Re_p^{0.687}}{1 + 0.15 Re_p^{0.687}} I^{0.858} Re_\lambda^{0.474}, \quad (48)$$

$$C'_{D,rms} = \frac{24}{Re'_p} \left[ 1 + 0.15 Re_p^{0.687} \left( 1.702 + 0.556 I^{-0.891} \left( \frac{D_p}{\eta} \right)^{0.111} \right) \right], \quad (49)$$

$$T_D = \frac{0.634 Re_\lambda^{0.654}}{1 + 4.614 e^{-2.282I}} \tau_\eta. \quad (50)$$

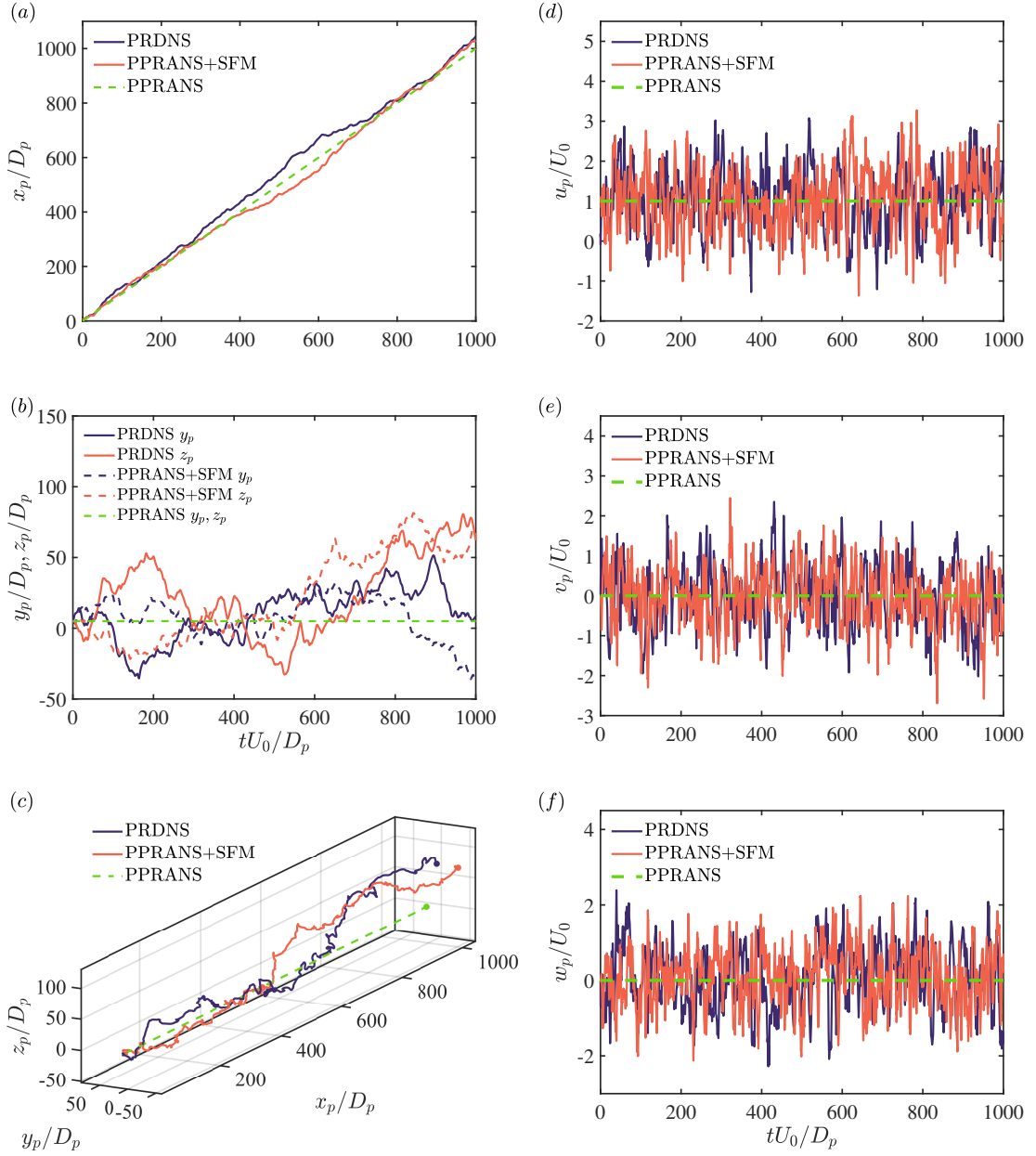


**Figure 17:** Time variations of (a,b,c) particle trajectories and (d,e,f) velocities with  $Re_{\rho_0} = 100$ ,  $I = 1.0$  and  $D_p/\eta = 22.2$ .

For PPRANS, the equations of particle motion are

$$\frac{d\mathbf{x}_p}{dt} = \mathbf{v}_p, \quad (51)$$

$$\frac{d\mathbf{v}_p}{dt} = \left(1 + 0.15Re_p^{0.687}\right) \frac{\mathbf{U} - \mathbf{v}_p}{\tau_p}. \quad (52)$$



**Table 3**

The relative errors of the mean and RMS particle velocities of the PPRANS+SFM prediction (the data in the bracket represent the relative errors of the PPRANS prediction).

Case	$\bar{u}_p$	$u_{p,rms}$	$v_{p,rms}$	$w_{p,rms}$
1	2.0% (3.1%)	0.9% (100%)	6.5% (100%)	5.8% (100%)
2	2.1% (2.3%)	3.7% (100%)	5.3% (100%)	7.3% (100%)
3	0.3% (0.3%)	7.1% (100%)	4.5% (100%)	8.9% (100%)
4	1.0% (1.1%)	4.7% (100%)	3.7% (100%)	5.2% (100%)
5	4.2% (6.2%)	1.8% (100%)	0.8% (100%)	3.9% (100%)
6	1.9% (6.2%)	5.9% (100%)	8.9% (100%)	7.5% (100%)
7	0.4% (6.2%)	1.9% (100%)	0.7% (100%)	5.9% (100%)
8	3.5% (3.8%)	5.0% (100%)	9.5% (100%)	7.4% (100%)

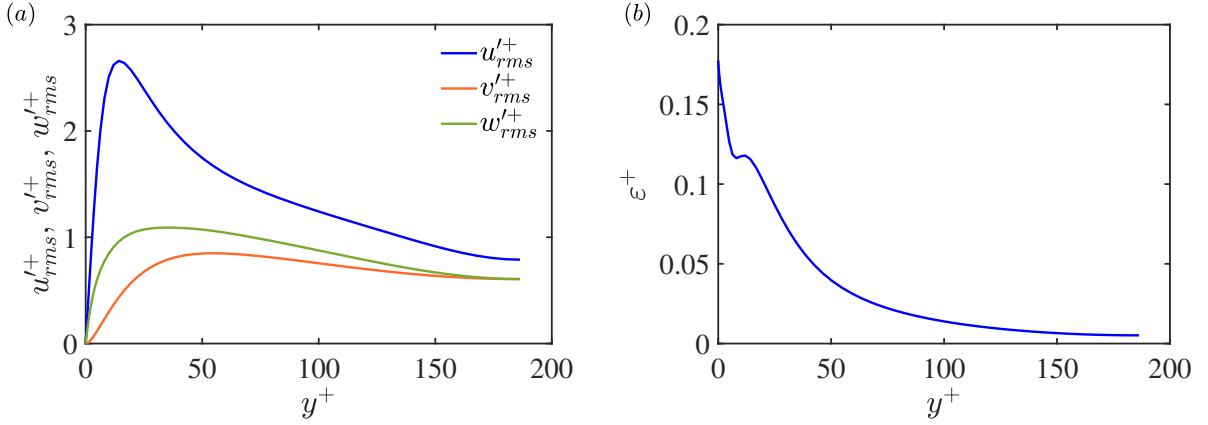
Here  $\mathbf{x}_p$  is the particle position,  $\mathbf{v}_p$  the particle velocity,  $\mathbf{U}$  the mean flow velocity, and  $\tau_p = (\rho_p D_p^2)/(18\rho_f \nu)$  the particle relaxation time. The stochastic model for the fluctuating drag force is adopted in all three directions. Moreover, the time advance of the particle motion is based on the second-order Adams-Bashforth scheme.

Figure 17 shows the time variations in the position, velocity, and trajectory of the particles from the results of the PRDNS, PPRANS, and PPRANS+SFM simulations with  $Re_{\rho 0} = 100$ ,  $I = 1.0$  and  $D_p/\eta = 22.2$  as an example. First, from the PPRANS result, it is clear that the particle moves along the streamwise direction steadily as the mean flow is in streamwise. The trajectory of the particle is a straight line and the particle does not have transverse motion. There are also no fluctuations in particle velocities because of the lack of turbulence effect in the PPRANS model. Second, with the PPRANS+SFM model, the turbulence effect is reasonably incorporated, and the fluctuations in particle trajectory and velocities can be well predicted, which are in qualitatively good agreement with the PRDNS result. To quantify the prediction errors of the stochastic model, table 3 displays the relative errors of the mean and RMS particle velocities predicted by the PPRANS+SFM as well as PPRANS to the PRDNS result. It can be seen that the overall relative errors of the mean and RMS particle velocities predicted by the PPRANS+SFM simulations are less than 10% for all cases. This indicates that the proposed stochastic model can accurately predict the first- and second-order particle statistics in turbulence.

#### 4.2. Particle dispersion in a turbulent channel flow

The second problem is the dispersion of small inertial particles in a turbulent channel flow. The friction Reynolds number is  $Re_\tau = u_\tau H/\nu = 180$ , where  $u_\tau = (\tau_w/\rho_f)^{1/2}$  is the friction velocity ( $\tau_w$  is the mean wall-shear stress,  $\rho_f$  is the fluid density),  $H$  is the half-height of the channel, and  $\nu$  is the fluid kinematic viscosity. The particle Stokes number  $St = (\rho_p D_p^2 u_\tau^2)/(18\rho_f \nu^2)$  is set to 25, 50, and 100, respectively, where the particle-to-fluid density ratio  $\rho_p/\rho_f$  is 2650. The particle size is very small, *i.e.*  $D_p^+ = 0.41, 0.58$  and  $0.82$ , therefore, PPDNS is performed for reference. There are 30000 particles in each case, and the particles are initially evenly distributed in the channel, and only the S-N drag force is considered in PPDNS. In addition, the particle concentration is very dilute, and the mean volume fractions are  $\phi_v = 1.2 \times 10^{-6}, 3.4 \times 10^{-6}$ , and  $9.5 \times 10^{-6}$ , respectively. Therefore, one-way coupling is assumed. The central difference scheme is utilized for the spatial discretization of the Navier-Stokes equations. The Adams-Bashforth scheme is employed for the convection term, while the Crank-Nicolson method is applied to the viscous term for time advancement. The size of the simulation domain is  $L_x \times L_y \times L_z = 4\pi H \times 2H \times 2\pi H$  and the grid number is  $256 \times 256 \times 192$ . The grid spacings in the streamwise and spanwise directions are uniform with  $\Delta x^+ = 8.84$  and  $\Delta z^+ = 5.89$ . In the wall-normal direction, the grid is finer near the wall and coarser near the center of the channel, with  $\Delta y^+ = 0.43 \sim 2.33$ .

Turbulent channel flow is highly anisotropic, which means that the intensities of turbulence fluctuation in different directions are quite different. To introduce the effect of turbulence anisotropy in our model, we use the turbulence intensities  $u'_{rms}, v'_{rms}$  and  $w'_{rms}$  in the  $x, y$  and  $z$  directions to replace the isotropic turbulence intensity  $u_{rms}$  in equation (46) in each direction. Furthermore, the turbulence-velocity-based particle Reynolds numbers and turbulence intensity



**Figure 18:** Profiles of (a) the turbulent velocity fluctuation intensities and (b) TDR along the wall-normal direction.

ratios in the three directions involved in equations (49) and (50) are introduced by

$$Re'_{p,x} = \frac{u'_{rms} D_p}{\nu}, \quad Re'_{p,y} = \frac{v'_{rms} D_p}{\nu}, \quad Re'_{p,z} = \frac{w'_{rms} D_p}{\nu}, \quad (53)$$

and

$$I_x = \frac{u'_{rms}}{|\mathbf{U} - \mathbf{v}_p|}, \quad I_y = \frac{v'_{rms}}{|\mathbf{U} - \mathbf{v}_p|}, \quad I_z = \frac{w'_{rms}}{|\mathbf{U} - \mathbf{v}_p|}. \quad (54)$$

The profiles of the turbulent velocity fluctuations and TDR along the wall-normal direction are shown in figure 18, where  $u'^+_{rms} = u'_{rms}/u_\tau$ ,  $v'^+_{rms} = v'_{rms}/u_\tau$ ,  $w'^+_{rms} = w'_{rms}/u_\tau$ ,  $\epsilon^+ = \epsilon\nu/u_\tau^4$  and  $y^+ = yu_\tau/\nu$ .

In this section, in addition to PPDNS and PPRANS+SFM, we also investigate the dispersion of particles in the channel flow utilizing a continuous random walk (CRW) model (Dehbi, 2008, 2010). This model utilizes statistical flow characteristics obtained from RANS to generate the fluctuating velocities of the flow encountered by particles via a stochastic model in the Lagrangian framework. Therefore, we will refer to it as "PPRANS+CRW". For PPRANS+CRW, the equations of particle motion are

$$\frac{d\mathbf{v}_p}{dt} = \left(1 + 0.15Re_p^{0.687}\right) \frac{(\mathbf{U} + \mathbf{u}') - \mathbf{v}_p}{\tau_p}, \quad (55)$$

in which  $\mathbf{u}'$  is the flow fluctuating velocities encountered by particle and defined as

$$d\left(\frac{u_1}{\sigma_1}\right) = -\left(\frac{u_1}{\sigma_1}\right) \cdot \frac{dt}{\tau_L} + \sqrt{\frac{2}{\tau_L}} \cdot dW_1 + \frac{\partial\left(\frac{u_1 u_2}{\sigma_1}\right)}{\partial x_2} \cdot \frac{dt}{1 + St_k}, \quad (56)$$

$$d\left(\frac{u_2}{\sigma_2}\right) = -\left(\frac{u_2}{\sigma_2}\right) \cdot \frac{dt}{\tau_L} + \sqrt{\frac{2}{\tau_L}} \cdot dW_2 + \frac{\partial\sigma_2}{\partial x_2} \cdot \frac{dt}{1 + St_k}, \quad (57)$$

$$d\left(\frac{u_3}{\sigma_3}\right) = -\left(\frac{u_3}{\sigma_3}\right) \cdot \frac{dt}{\tau_L} + \sqrt{\frac{2}{\tau_L}} \cdot dW_3, \quad (58)$$

where the subscripts 1, 2, and 3 represent the streamwise, vertical and spanwise directions,  $u_i$  is the component of  $\mathbf{u}'$  in the  $i$ th direction,  $\sigma_i$  is the RMS of the flow velocity fluctuation,  $dW_i$  is the discrete Wiener process,  $\tau_L = \tau_L^+ \nu/u_\tau$ ,

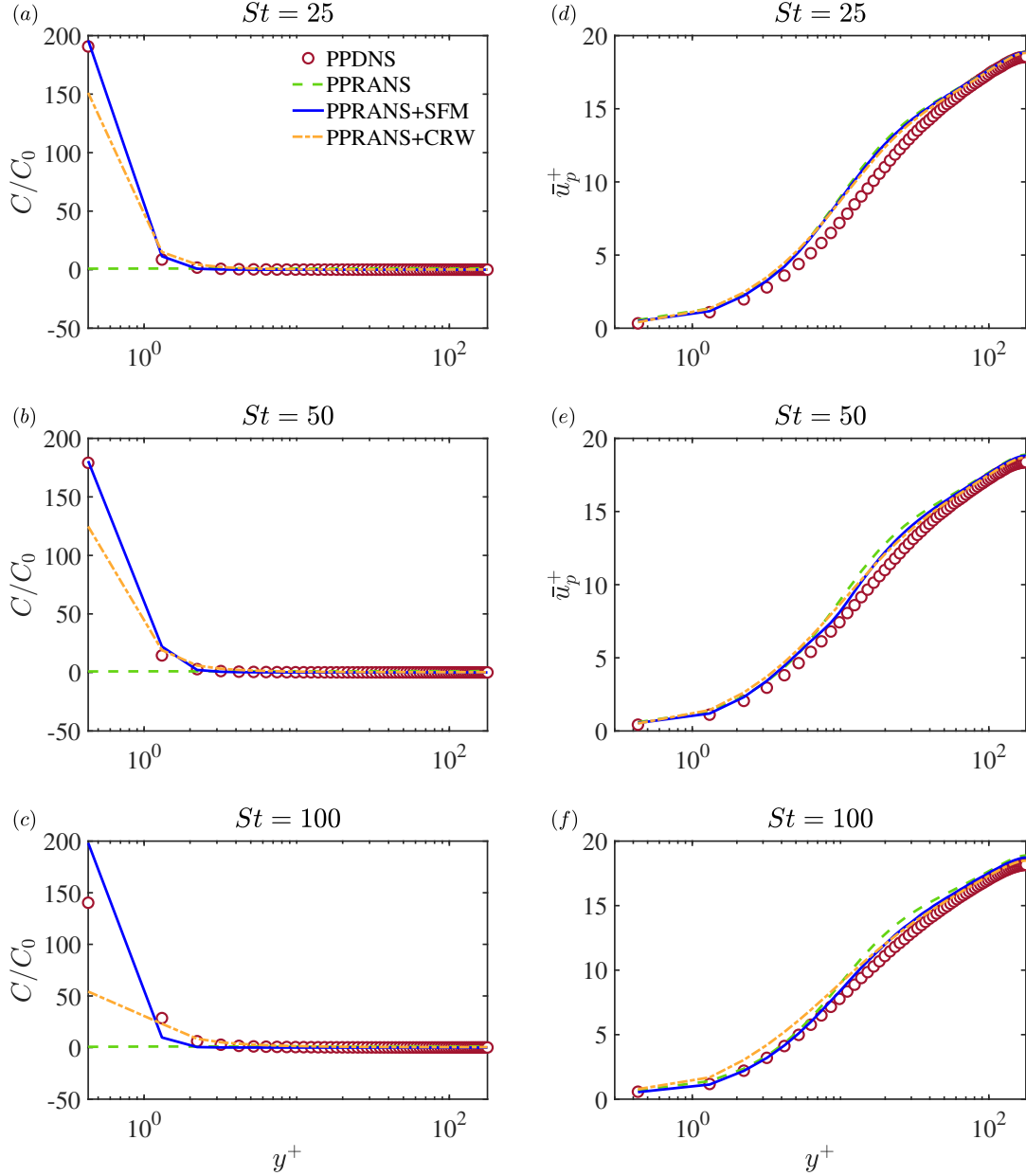


**Figure 19:** Profiles of (a,b,c) the normalized particle concentration and (d,e,f) the particle mean streamwise velocity along the wall-normal direction with different particle Stokes numbers.

and  $\tau_L^+$  is approximated by the fit obtained by [Kallio and Reeks \(1989\)](#) as

$$\tau_L^+ = \begin{cases} 10, & y^+ \leq 5, \\ 7.122 + 0.5731y^+ - 0.00129y^{+2}, & 5 < y^+ < 200. \end{cases} \quad (59)$$

And  $St_k = \tau_p / \tau_L$ .

Figure 19 shows the profiles of the mean particle concentration and the mean streamwise particle velocity along the wall-normal direction with different particle Stokes numbers, where  $C$  is the mean particle concentration and  $C_0$  is the bulk concentration. It can be seen that if the stochastic force contributions due to turbulence are not considered

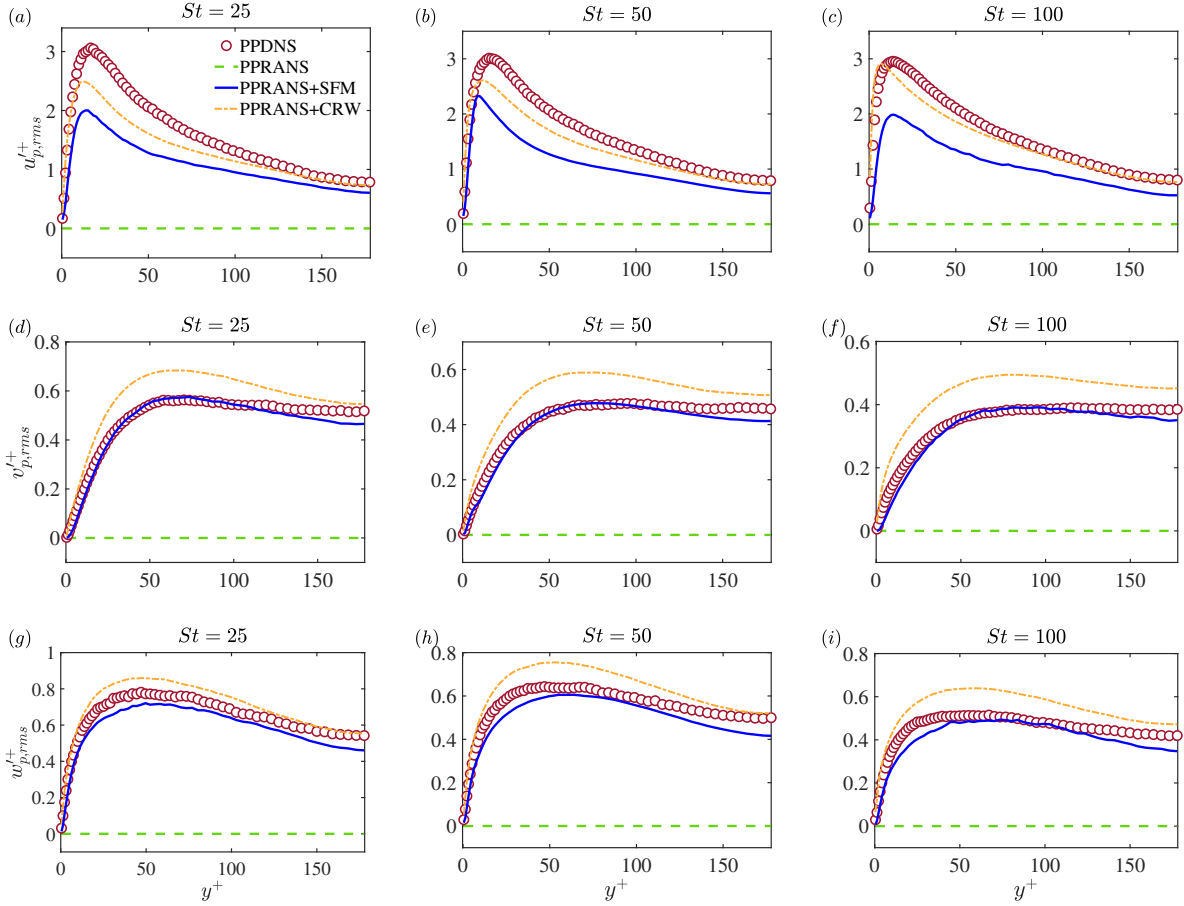


**Figure 20:** Profiles of the (a,b,c) streamwise, (d,e,f) wall-normal and (g,h,i) spanwise particle velocity fluctuation intensities along the wall-normal direction with different particle Stokes numbers.

(PPRANS), the particles are evenly distributed along the wall-normal direction, and there is no accumulation of particles near the wall caused by turbophoresis as observed in PPDNS. In contrast, PPRANS+SFM can predict the near-wall accumulation of particles, and the particle concentration distributions along the wall in the wall-normal direction coincide well with the PPDNS results. Moreover, in figure 19 (d,e,f), it can be seen that the mean particle streamwise velocity profiles predicted by PPRANS+SFM are also in good agreement with the PPDNS results. Figure 20 displays the profiles of the fluctuations in particle velocity along the wall-normal direction. It is seen that the predictions of PPRANS+SFM agree well with the results of PPDNS, especially for the wall-normal and spanwise particle velocity fluctuations. There are some discrepancies in the streamwise particle velocity fluctuations, which require further investigations and improvements in the future. Due to the lack of turbulence effects, PPRANS cannot predict particle velocity fluctuations. Furthermore, as illustrated in figure 19, PPRANS+CRW also demonstrates good performance in predicting the mean concentration and mean velocity of the particles. However, it exhibits relatively inferior accuracy in predicting particle concentration near the wall compared to PPRANS+SFM. Additionally, figure 20 indicates that while PPRANS+CRW excels at predicting particle streamwise velocity fluctuations, PPRANS+SFM provides more accurate predictions of particle spanwise and wall-normal velocity fluctuations.

### 4.3. Summary of the validation study

The results of the two validation problems indicate that the proposed stochastic force models can accurately predict particle statistics in isotropic and anisotropic turbulence for both finite-size and point particles. To apply the stochastic force model, the mean flow velocity, TKE, and TDR must be known *a priori*, which can be given from DNS data or

RANS simulation using a specific turbulence closure, such as the  $k - \varepsilon$  or  $k - \omega$  model. If the effect of turbulence anisotropy needs to be included, more complicated Reynolds stress models can be adopted.

## 5. Conclusions

This study conducts a series of direct numerical simulations to accurately compute the drag and lateral fluid forces on a fixed particle in homogeneous and isotropic turbulence superimposed with a uniform flow over a wide range of parameters: the particle Reynolds number is 0.1~300, the scale ratio between the particle size and the Kolmogorov scale of turbulence is 0.22~76.9, and the turbulence intensity ratio is 0.1~20. The background turbulence is kept in a statistically steady state, and the particle wake effect is eliminated by a concurrent precursor technique. Stochastic models based on the Langevin equation for the drag and lateral fluid forces were proposed with the high-fidelity PRDNS data. The proposed models were validated in two problems: the motion of a finite-sized particle in turbulence and the dispersion of small inertial particles in a turbulent channel flow. The predictions of the proposed stochastic models exhibit remarkable consistency with the DNS results in both cases. The inputs of the current model consist of the distributions of the mean flow velocity, the mean kinetic energy of the turbulence, and the mean turbulent dissipation rate, which can be effectively provided by various RANS turbulence closures. Consequently, it can be utilized for numerous particle-laden flow problems while maintaining an acceptable computational cost.

Several issues need further discussion. First, the particle is fixed in our PRDNS, indicating that the particle has an infinite response time  $\tau_p$ . Therefore, the proposed force model can only be reliably applied for highly inertial particles with  $St \gg 1$  and  $\rho_p/\rho_f \gg 1$  ( $\rho_p$  and  $\rho_f$  are the densities of particle and fluid, respectively). In other words, the model cannot be used for particles whose density is close to or smaller than that of the fluid, *e.g.* tracer particles. It is also outside the scope of some specific theories for idealized inertialess particles, such as the Tchen-Hinze theory (Hinze, 1975). Second, if we assume that there is a high particle-to-fluid density ratio, then the drag force is the most important, and other forces, such as the added mass and Basset history forces, can be neglected. To relieve the limits of the large density ratio assumption, one can simulate freely evolving particle suspensions in turbulent flows and develop new drag correlations (Tang, Peters and Kuipers, 2016; Tavanashad, Passalacqua, Fox and Subramaniam, 2019; Tavanashad et al., 2021), which are left for future studies. Third, we only consider one-way coupling in the applications of the model, as the disperse phase is dilute. An extension to two-way coupling should be straightforward, and we will consider it in future works. The wake removal method is not responsible for the fluid-particle coupling, which should be essentially determined by the volume fraction or mass loading of the disperse phase.

## CRedit authorship contribution statement

**Yuqi Wang:** Methodology, Software, Analysis and Writing. **Ruifeng Hu:** Conceptualization, Methodology, Software, Analysis and Writing.

## Acknowledgement

The authors acknowledge the financial support from the National Natural Science Foundation of China (Nos. 12388101 and 12472221) and the Fundamental Research Funds for the Central Universities (lzujbky-2024-oy10).

## Appendix A. Simulation parameters

Table 4 lists the simulation parameters of a fixed particle in turbulence described in section 2.4.

## Appendix B. Influence of the particle wake removing method and domain size

Two types of boundary conditions are adopted to calculate the drag coefficient of the particles in uniform inflow. In the first type, the inlet and outlet boundary conditions are applied in the streamwise direction, while the free-slip boundary conditions were used in the two transverse directions. In the second type, periodic boundary conditions were applied in all three directions, and the concurrent precursor method is also employed to remove the particle wake. In both types, the computational domain size is  $L_x \times L_y \times L_z = 20D_p \times 10D_p \times 10D_p$ , the particle is fixed at  $\mathbf{x}_p = (5D_p, 5D_p, 5D_p)$ , and the grid size is  $h = D_p/20$ . The particle Reynolds numbers are 1, 10, 40, 100, 200 and

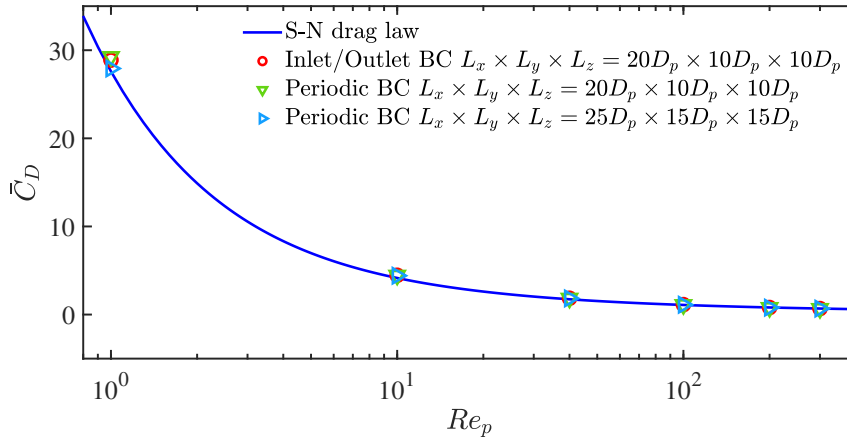


**Figure 21:** Comparison of the mean drag coefficient of a particle in a uniform flow by PRDNS and the S–N drag law.

300. In addition, another case using the periodic boundary condition with a larger domain size of  $L_x \times L_y \times L_z = 25D_p \times 15D_p \times 15D_p$  (the particle is fixed at  $\mathbf{x}_p = (5D_p, 7.5D_p, 7.5D_p)$ ) is carried out to check the domain independence. Figure 21 shows the comparison of the mean drag coefficients of PRDNS with the two types of boundary conditions and the S–N drag law. It can be seen that the mean particle drag coefficients are in good agreement with the S–N drag law, and the maximum error is less than 10% for both boundary conditions. This demonstrates the feasibility of the concurrent precursor method used in this study and confirms the independence of the domain size.

## References

- Akiki, G., Jackson, T.L., Balachandar, S., 2017a. Pairwise interaction extended point-particle model for a random array of monodisperse spheres. *J. Fluid Mech.* 813, 882–928.
- Akiki, G., Moore, W.C., Balachandar, S., 2017b. Pairwise-interaction extended point-particle model for particle-laden flows. *J. Comput. Phys.* 351, 329–357.
- Armenio, V., Fiorotto, V., 2001. The importance of the forces acting on particles in turbulent flows. *Phys. Fluids* 13, 2437–2440.
- Bagchi, P., Balachandar, S., 2003. Effect of turbulence on the drag and lift of a particle. *Phys. Fluids* 15, 3496–3513.
- Balachandar, S., 2009. A scaling analysis for point–particle approaches to turbulent multiphase flows. *Int. J. Multiph. Flow* 35, 801–810.
- Balachandar, S., Eaton, J.K., 2010. Turbulent dispersed multiphase flow. *Ann. Rev. Fluid Mech.* 42, 111–133.
- Balachandar, S., Moore, W.C., Akiki, G., Liu, K., 2020. Toward particle-resolved accuracy in Euler–Lagrange simulations of multiphase flow using machine learning and pairwise interaction extended point-particle (PIEP) approximation. *Theor. Comput. Fluid Dyn.* 34, 401–428.
- Balachandar, S., Peng, C., Wang, L.P., 2024. Turbulence modulation by suspended finite-sized particles: Toward physics-based multiphase subgrid modeling. *Phys. Rev. Fluids* 9, 044304.
- Bassenne, M., Esmaily, M., Livescu, D., Moin, P., Urzay, J., 2019. A dynamic spectrally enriched subgrid-scale model for preferential concentration in particle-laden turbulence. *Int. J. Multiph. Flow* 116, 270–280.
- Bassenne, M., Urzay, J., Park, G.I., Moin, P., 2016. Constant-energetics physical-space forcing methods for improved convergence to homogeneous-isotropic turbulence with application to particle-laden flows. *Phys. Fluids* 28, 035114.
- Beetstra, R., van der Hoef, M.A., Kuipers, J.A.M., 2007. Drag force of intermediate Reynolds number flow past mono- and bidisperse arrays of spheres. *AIChE J.* 53, 489–501.
- Berrouk, A.S., Laurence, D., Riley, J.J., Stock, D.E., 2007. Stochastic modelling of inertial particle dispersion by subgrid motion for LES of high Reynolds number pipe flow. *J. Turbul.* 8, 1–20.
- Bocksell, T.L., Loth, E., 2001. Random walk models for particle diffusion in free-shear flows. *AIAA J.* 39, 1086–1096.
- Bocksell, T.L., Loth, E., 2006. Stochastic modeling of particle diffusion in a turbulent boundary layer. *Int. J. Multiph. Flow* 32, 1234–1253.
- Brandt, L., Coletti, F., 2022. Particle-laden turbulence: Progress and perspectives. *Ann. Rev. Fluid Mech.* 54, 159–189.
- Breugem, W.P., 2012. A second-order accurate immersed boundary method for fully resolved simulations of particle-laden flows. *J. Comput. Phys.* 231, 4469–4498.
- Brucato, A., Grisafi, F., Montante, G., 1998. Particle drag coefficients in turbulent fluids. *Chem. Eng. Sci.* 53, 3295–3314.
- Burton, T.M., Eaton, J.K., 2005. Fully resolved simulations of particle-turbulence interaction. *J. Fluid Mech.* 545, 67–111.
- Cate, A.T., Sundaresan, S., 2006. Analysis of unsteady forces in ordered arrays of monodisperse spheres. *J. Fluid Mech.* 552, 257–287.
- Cernick, M.J., Tullis, S.W., Lightstone, M.F., 2015. Particle subgrid scale modelling in large-eddy simulations of particle-laden turbulence. *J. Turbul.* 16, 101–135.



- Cheng, Z., Wachs, A., 2023a. Hydrodynamic force and torque fluctuations in a random array of polydisperse stationary spheres. *Int. J. Multiph. Flow* 167, 104524.
- Cheng, Z., Wachs, A., 2023b. Physics-informed neural network for modelling force and torque fluctuations in a random array of bidisperse spheres. *Int. J. Multiph. Flow* 169, 104603.
- Constantinescu, G.S., Squires, K.D., 2003. LES and DES investigations of turbulent flow over a sphere at  $Re = 10,000$ . *Flow Turbul. Combust.* 70, 267–298.
- Costa, P., Brandt, L., Picano, F., 2020. Interface-resolved simulations of small inertial particles in turbulent channel flow. *J. Fluid Mech.* 883, A54.
- Costa, P., Brandt, L., Picano, F., 2021. Near-wall turbulence modulation by small inertial particles. *J. Fluid Mech.* 922, A9.
- Crowe, C.T., Troutt, R., Chung, N., 1996. Numerical models for two-phase turbulent flows. *Ann. Rev. Fluid Mech.* 28, 11–43.
- Dehbi, A., 2008. Turbulent particle dispersion in arbitrary wall-bounded geometries: A coupled CFD-Langevin-equation based approach. *Int. J. Multiph. Flow* 34, 819–828.
- Dehbi, A., 2010. Validation against DNS statistics of the normalized Langevin model for particle transport in turbulent channel flows. *Powder Technol.* 200, 60–68.
- Draw, D.A., 1983. Mathematical modeling of two-phase flow. *Ann. Rev. Fluid Mech.* 15, 261–291.
- Eaton, J.K., 2009. Two-way coupled turbulence simulations of gas-particle flows using point-particle tracking. *Int. J. Multiph. Flow* 35, 792–800.
- Elghobashi, S., 1994. On predicting particle-laden turbulent flows. *Appl. Sci. Res.* 52, 309–329.
- Elghobashi, S., 2019. Direct numerical simulation of turbulent flows laden with droplets or bubbles. *Annu. Rev. Fluid Mech.* 51, 217–244.
- Elmestikawy, H., Chéron, V., van Wachem, B., 2025. On the influence of the periodic boundary conditions on the drag of random particle arrangements in PR-DNS. *Int. J. Multiph. Flow* 185, 105143.
- Esteghamatian, A., Euzenat, F., Hammouti, A., Lance, M., Wachs, A., 2018. A stochastic formulation for the drag force based on multiscale numerical simulation of fluidized beds. *Int. J. Multiph. Flow* 99, 363–382.
- Fede, P., Simonin, O., 2006. Numerical study of the subgrid fluid turbulence effects on the statistics of heavy colliding particles. *Phys. Fluids* 18, 045103.
- Fox, R.O., 2012. Large-eddy-Simulation tools for multiphase flows. *Ann. Rev. Fluid Mech.* 44, 47–76.
- Fox, R.O., 2024. Recent advances in well-posed Eulerian models for polydisperse multiphase flows. *Int. J. Multiph. Flow* 172, 104715.
- Garzó, V., Tenneti, S., Subramaniam, S., Hrenya, C.M., 2012. Enskog kinetic theory for monodisperse gas–solid flows. *J. Fluid Mech.* 712, 129–168.
- Gatignol, R., 1983. The Faxén formulae for a rigid particle in an unsteady non-uniform stokes flow. *J. Mécanique Théorique Appl.* 2, 143–160.
- Glowinski, R., Pan, T.W., Hesla, T.I., Joseph, D.D., 1999. A distributed Lagrange multiplier/fictitious domain method for particulate flows. *Int. J. Multiph. Flow* 25, 755–794.
- Glowinski, R., Pan, T.W., Hesla, T.I., Joseph, D.D., Periaux, J., 2001. A fictitious domain approach to the direct numerical simulation of incompressible viscous flow past moving rigid bodies: application to particulate flow. *J. Comput. Phys.* 169, 363–426.
- Gong, Z., Wu, Z., An, C.G., Zhang, B.W., Fu, X., 2023. CP3d: A comprehensive Euler-Lagrange solver for direct numerical simulation of particle-laden flows. *Comput. Phys. Comm.* 286, 108666.
- Gosman, A.D., Ioannides, E., 1983. Aspects of computer simulation of liquid-fueled combustors. *J. Ener.* 7, 482–490.
- Hausmann, M., Evrard, F., van Wachem, B., 2023a. Large eddy simulation model for two-way coupled particle-laden turbulent flows. *Phys. Rev. Fluids* 8, 084301.
- Hausmann, M., Evrard, F., van Wachem, B., 2023b. Wavelet-based modeling of subgrid scales in large-eddy simulation of particle-laden turbulent flows. *Phys. Rev. Fluids* 8, 104604.
- Hill, R.J., Koch, D.L., Ladd, A.J.C., 2001. Moderate-Reynolds-number flows in ordered and random arrays of spheres. *J. Fluid Mech.* 448, 243–278.
- Hinze, J.O., 1975. *Turbulence*. McGraw-Hill Book Company.
- Van der Hoef, M.A., Beetstra, R., Kuipers, J.A., 2005. Lattice-Boltzmann simulations of low-Reynolds-number flow past mono- and bidisperse arrays of spheres: Results for the permeability and drag force. *J. Fluid Mech.* 528, 233–254.
- Homann, H., Bec, J., Grauer, R., 2013. Effect of turbulent fluctuations on the drag and lift forces on a towed sphere and its boundary layer. *J. Fluid Mech.* 721, 155–179.
- Huang, W.X., Tian, F.B., 2019. Recent trends and progress in the immersed boundary method. *Proc. Inst. Mech. Eng., Part C* 233, 7617–7636.
- Innocenti, A., Fox, R.O., Salvetti, M.V., Chibbaro, S., 2019. A Lagrangian probability-density-function model for collisional turbulent fluid-particle flows. *J. Fluid Mech.* 862, 449–489.
- Innocenti, A., Marchioli, C., Chibbaro, S., 2016. Lagrangian filtered density function for LES-based stochastic modelling of turbulent particle-laden flows. *Phys. Fluids* 28, 115106.
- Jaiswal, A., Bui, M.D., Rutschmann, P., 2022. Evaluation of RANS-DEM and LES-DEM methods in OpenFOAM for simulation of particle-laden turbulent flows. *Fluids* 7, 141–151.
- Ji, C., Munjiza, A., Avital, E., Ma, J., Williams, J.J.R., 2013. Direct numerical simulation of sediment entrainment in turbulent channel flow. *Phys. Fluids* 056601.
- Ji, C., Munjiza, A., Avital, E., Xu, D., Williams, J., 2014. Saltation of particles in turbulent channel flow. *Phys. Rev. E* 89, 1–14.
- Jin, G., He, G., Wang, L.P., Zhang, J., 2010. Subgrid scale fluid velocity timescales seen by inertial particles in large-eddy simulation of particle-laden turbulence. *Int. J. Multiph. Flow* 36, 432–437.
- Johnson, T.A., Patel, V.C., 1999. Flow past a sphere up to a Reynolds number of 300. *J. Fluid Mech.* 378, 19–70.
- Kallio, G., Reeks, M., 1989. A numerical simulation of particle deposition in turbulent boundary layers. *Int. J. Multiph. Flow* 15, 433–446.
- Kempe, T., Fröhlich, J., 2012. An improved immersed boundary method with direct forcing for the simulation of particle laden flows. *J. Comput. Phys.* 231, 3663–3684.
- Kidanemariam, A.G., Chan-Braun, C., Doychev, T., Uhlmann, M., 2013. Direct numerical simulation of horizontal open channel flow with finite-size, heavy particles at low solid volume fraction. *New J. Phys.* 15, 025031.
- Kidanemariam, A.G., Uhlmann, M., 2014a. Direct numerical simulation of pattern formation in subaqueous sediment. *J. Fluid Mech.* 750, R2.

- Kidanemariam, A.G., Uhlmann, M., 2014b. Interface-resolved direct numerical simulation of the erosion of a sediment bed sheared by laminar channel flow. *Int. J. Multiph. Flow* 67, 174–188.
- Kidanemariam, A.G., Uhlmann, M., 2017. Formation of sediment patterns in channel flow: minimal unstable systems and their temporal evolution. *J. Fluid Mech.* 818, 716–743.
- Kim, D., Choi, H., 2002. Laminar flow past a sphere rotating in the streamwise direction. *J. Fluid Mech.* 461, 365–386.
- Kim, J., Balachandar, S., 2012. Mean and fluctuating components of drag and lift forces on an isolated finite-sized particle in turbulence. *Theor. Comput. Fluid Dyn.* 26, 185–204.
- Kim, J., Kim, D., Choi, H., 2001. An immersed-boundary finite-volume method for simulations of flow in complex geometries. *J. Comput. Phys.* 171, 132–150.
- Kim, J., Moin, P., 1985. Application of a fractional-step method to incompressible Navier-Stokes equations. *J. Comput. Phys.* 59, 308–323.
- Knorps, M., Pozorski, J., 2021. Stochastic modeling for subgrid-scale particle dispersion in large-eddy simulation of inhomogeneous turbulence. *Phys. Fluids* 33, 043323.
- Kraichnan, R.H., 1970. Diffusion by a random velocity field. *Phys. Fluids* 13, 22–31.
- Kuerten, J.G.M., 2006. Subgrid modeling in particle-laden channel flow. *Phys. Fluids* 18, 025108.
- Kuerten, J.G.M., 2016. Point-particle DNS and LES of particle-laden turbulent flow - a state-of-the-art review. *Flow Turbul. Combust.* 97, 689–713.
- Langevin, P., 1908. Sur la théorie du mouvement brownien. *Comptes Rendus Acad* 146, 530–533.
- Lattanzi, A.M., Tavanashad, V., Subramaniam, S., Capecelatro, J., 2020. Stochastic models for capturing dispersion in particle-laden flows. *J. Fluid Mech.* 903, A7.
- Lattanzi, A.M., Tavanashad, V., Subramaniam, S., Capecelatro, J., 2022. Stochastic model for the hydrodynamic force in Euler–Lagrange simulations of particle-laden flows. *Phys. Rev. Fluids* 7, 014301.
- Li, W., Shi, H., Yu, X., 2023. An improvement to continuous random walk model for sediment diffusion in inhomogeneous turbulent flows. *Environ. Fluid Mech.* 23, 779–797.
- Liska, S., Colonius, T., 2017. A fast immersed boundary method for external incompressible viscous flows using lattice Green's functions. *J. Comput. Phys.* 331, 257–279.
- Lo, C., Bons, J., Yao, Y., Capecelatro, J., 2022. Assessment of stochastic models for predicting particle transport and deposition in turbulent pipe flows. *J. Aerosol Sci.* 162, 105954.
- Loth, E., 2000. Numerical approaches for motion of dispersed particles, droplets and bubbles. *Prog. Ener. Combust. Sci.* 26, 161–223.
- Loth, E., Dorgan, A.J., 2009. An equation of motion for particles of finite Reynolds number and size. *Environ. Fluid Mech.* 9, 187–206.
- Luo, K., Hu, C., Wu, F., Fan, J., 2017. Direct numerical simulation of turbulent boundary layer with fully resolved particles at low volume fraction. *Phys. Fluids* 29, 053301.
- Luo, K., Wang, Z., Fan, J., Cen, K., 2007. Full-scale solutions to particle-laden flows: Multidirect forcing and immersed boundary method. *Phys. Rev. E* 76, 066709.
- Marchioli, C., 2017. Large-eddy simulation of turbulent dispersed flows: a review of modelling approaches. *Acta Mech.* 228, 741–771.
- Marchioli, C., Salvetti, M.V., Soldati, A., 2008a. Appraisal of energy recovering sub-grid scale models for large-eddy simulation of turbulent dispersed flows. *Acta Mech.* 201, 277–296.
- Marchioli, C., Salvetti, M.V., Soldati, A., 2008b. Some issues concerning large-eddy simulation of inertial particle dispersion in turbulent bounded flows. *Phys. Fluids* 20, 040603.
- Maxey, M., 2017. Simulation methods for particulate flows and concentrated suspensions. *Ann. Rev. Fluid Mech.* 49, 171–193.
- Maxey, M.R., Riley, J.J., 1983. Equation of motion for a small rigid sphere in a nonuniform flow. *Phys. Fluids* 26, 883–889.
- Mazzuoli, M., Blondeaux, P., Vittori, G., Uhlmann, M., Simeonov, J., Calantoni, J., 2020. Interface-resolved direct numerical simulations of sediment transport in a turbulent oscillatory boundary layer. *J. Fluid Mech.* 885, A28.
- McLaughlin, J.B., 1994. Numerical computation of particles-turbulence interaction. *Int. J. Multiph. Flow* 20, 211–232.
- Michaelides, E., 1997. Review - the transient equation of motion for particles, bubbles, and droplets. *J. Fluids Eng.* 119, 233–247.
- Michaelides, E.E., 2003. Hydrodynamic force and heat/mass transfer from particles, bubbles, and drops - The Freeman scholar lecture. *J. Fluids Eng.* 125, 209–238.
- Minier, J.P., 2015. On Lagrangian stochastic methods for turbulent polydisperse two-phase reactive flows. *Prog. Ener. Combust. Sci.* 50, 1–62.
- Mittal, R., Iaccarino, G., 2005. Immersed boundary methods. *Ann. Rev. Fluid Mech.* 37, 239–261.
- Mittal, R., Seo, J.H., 2023. Origin and evolution of immersed boundary methods in computational fluid dynamics. *Phys. Rev. Fluids* 8, 100501.
- Mofakham, A.A., Ahmadi, G., 2019. Particles dispersion and deposition in inhomogeneous turbulent flows using continuous random walk models. *Phys. Fluids* 31, 083301.
- Mofakham, A.A., Ahmadi, G., 2020. On random walk models for simulation of particle-laden turbulent flows. *Int. J. Multiph. Flow* 122, 103157.
- Niazmand, H., Renksizbulut, M., 2003. Surface effects on transient three-dimensional flows around rotating spheres at moderate Reynolds numbers. *Comput. Fluids* 32, 1405–1433.
- Oka, S., Goto, S., 2022. Attenuation of turbulence in a periodic cube by finite-size spherical solid particles. *J. Fluid Mech.* 949, A45.
- Pan, Y., Banerjee, S., 1996. Numerical simulation of particle interactions with wall turbulence. *Phys. Fluids* 8, 2733–2755.
- Park, G.I., Bassenne, M., Urzay, J., Moin, P., 2017. A simple dynamic subgrid-scale model for les of particle-laden turbulence. *Phys. Rev. Fluids* 2, 1–20.
- Peng, C., Ayala, O.M., Wang, L.P., 2019. A direct numerical investigation of two-way interactions in a particle-laden turbulent channel flow. *J. Fluid Mech.* 875, 1096–1144.
- Peng, C., Ayala, O.M., Wang, L.P., 2020. Flow modulation by a few fixed spherical particles in a turbulent channel flow. *J. Fluid Mech.* 884, A15.
- Peng, C., Sun, Q., Wang, L.P., 2023. Parameterization of turbulence modulation by finite-size solid particles in forced homogeneous isotropic turbulence. *J. Fluid Mech.* 963, A6.
- Peng, C., Wang, L.P., 2023. Mechanisms and models of particle drag enhancements in turbulent environments. *J. Fluid Mech.* 959, A30.

- Peng, C., Wang, L.P., Chen, S., 2024. Preferential accumulation of finite-size particles in near-wall streaks. *J. Fluid Mech.* 980, A38.
- Picano, F., Breugem, W.P., Brandt, L., 2015. Turbulent channel flow of dense suspensions of neutrally buoyant spheres. *J. Fluid Mech.* 764, 463–487.
- Ploumhans, P., Winckelmans, G.S., Salmon, J.K., Leonard, A., Warren, M.S., 2002. Vortex methods for direct numerical simulation of three-dimensional bluff body flows: Application to the sphere at  $Re=300$ , 500, and 1000. *J. Comput. Phys.* 178, 427–463.
- Pope, S.B., 2000. *Turbulent Flows*. Cambridge University Press.
- Pozorski, J., 2017. *Particles in Wall-Bounded Turbulent Flows: Deposition, Re-Suspension and Agglomeration*. Springer International Publishing. chapter Models of Turbulent Flows and Particle Dynamics. pp. 97–150.
- Pozorski, J., Apte, S.V., 2009. Filtered particle tracking in isotropic turbulence and stochastic modeling of subgrid-scale dispersion. *Int. J. Multiph. Flow* 35, 118–128.
- Ray, B., Collins, L.R., 2014. A subgrid model for clustering of high-inertia particles in large-eddy simulations of turbulence. *J. Turbul.* 15, 366–385.
- Roma, A.M., Peskin, C.S., Berger, M.J., 1999. An adaptive version of the immersed boundary method. *J. Comput. Phys.* 153, 509–534.
- Rousta, F., Lessani, B., Ahmadi, G., 2024. Stochastic subgrid-scale modeling for particles dispersion and deposition for a filtered DNS channel flow field. *Int. J. Multiph. Flow* 175, 104801.
- Saad, T., Cline, D., Stoll, R., Sutherland, J.C., 2017. Scalable tools for generating synthetic isotropic turbulence with arbitrary spectra. *AIAA J.* 55, 327–331.
- Sabelnikov, V., Barge, A., Gorokhovski, M., 2019. Stochastic modeling of fluid acceleration on residual scales and dynamics of suspended inertial particles in turbulence. *Phys. Rev. Fluids* 4, 1–19.
- Scherer, M., Uhlmann, M., Kidanemariam, A.G., Krayer, M., 2022. On the role of turbulent large-scale streaks in generating sediment ridges. *J. Fluid Mech.* 930, A11.
- Schiller, L., Naumann, A., 1933. Über die grundlegenden berechnungen bei der schwerkraftaufbereitung. *Verein Deutscher Ingenieure* 77, 318–320.
- Schneiderbauer, S., 2024. Continuum modeling of gas–particle flows: an overview. *Acta Mech.* .
- Schwarzmeier, C., Rettinger, C., Kemmler, S., Plewinski, J., Núñez-González, F., Köstler, H., Råde, U., Vowinkel, B., 2023. Particle-resolved simulation of antidunes in free-surface flows. *J. Fluid Mech.* 961, R1.
- Seyed-Ahmadi, A., Wachs, A., 2020. Microstructure-informed probability-driven point-particle model for hydrodynamic forces and torques in particle-laden flows. *J. Fluid Mech.* 900, A21.
- Seyed-Ahmadi, A., Wachs, A., 2022. Physics-inspired architecture for neural network modeling of forces and torques in particle-laden flows. *Comput. Fluids* 238, 105379.
- Shao, X., Wu, T., Yu, Z., 2012. Fully resolved numerical simulation of particle-laden turbulent flow in a horizontal channel at a low Reynolds number. *J. Fluid Mech.* 693, 319–344.
- Shotorban, B., Mashayek, F., 2006a. A stochastic model for particle motion in large-eddy simulation. *J. Turbul.* 7, 1–13.
- Shotorban, B., Mashayek, F., 2006b. A stochastic model for particle motion in large-eddy simulation. *J. Turbul.* 7, 1–13.
- Soldati, A., Marchioli, C., 2009. Physics and modelling of turbulent particle deposition and entrainment: Review of a systematic study. *Int. J. Multiph. Flow* 35, 827–839.
- Stevens, R.J.A.M., Graham, J., Meneveau, C., 2014. A concurrent precursor inflow method for large eddy simulations and applications to finite length wind farms. *Renew. Energy* 68, 46–50.
- Subramaniam, S., 2013. Lagrangian-Eulerian methods for multiphase flows. *Prog. Ener. Combust. Sci.* 39, 215–245.
- Tang, Y., Peters, E.A.J.F., Kuipers, J.A.M., 2016. Direct numerical simulations of dynamic gas–solid suspensions. *AIChE J.* 62, 1958–1969.
- Tang, Y., Peters, E.A.J.F., Kuipers, J.A.M., Kriebitzsch, S.H.L., van der Hoef, M.A., 2015. A new drag correlation from fully resolved simulations of flow past monodisperse static arrays of spheres. *AIChE J.* 61, 688–698.
- Tanière, A., Arcen, B., 2016. Overview of existing Langevin models formalism for heavy particle dispersion in a turbulent channel flow. *Int. J. Multiph. Flow* 82, 106–118.
- Tao, S., Zhang, H., Guo, Z., Wang, L.P., 2018. A combined immersed boundary and discrete unified gas kinetic scheme for particle–fluid flows. *J. Comput. Phys.* 375, 498–518.
- Tavanashad, V., Passalacqua, A., Fox, R.O., Subramaniam, S., 2019. Effect of density ratio on velocity fluctuations in dispersed multiphase flow from simulations of finite-size particles. *Acta Mech.* 230, 469–484.
- Tavanashad, V., Passalacqua, A., Subramaniam, S., 2021. Particle-resolved simulation of freely evolving particle suspensions: Flow physics and modeling. *Int. J. Multiph. Flow* 135, 103533.
- Tenneti, S., Garg, R., Subramaniam, S., 2011. Drag law for monodisperse gas–solid systems using particle-resolved direct numerical simulation of flow past fixed assemblies of spheres. *Int. J. Multiph. Flow* 37, 1072–1092.
- Tenneti, S., Mehrabadi, M., Subramaniam, S., 2016. Stochastic Lagrangian model for hydrodynamic acceleration of inertial particles in gas–solid suspensions. *J. Fluid Mech.* 788, 695–729.
- Tenneti, S., Subramaniam, S., 2014. Particle-resolved direct numerical simulation for gas–solid flow model development. *Ann. Rev. Fluid Mech.* 46, 199–230.
- Tsai, S.T., 1957. Sedimentation motion of sand particles in moving water (I): The resistance on a small sphere moving in non-uniform flow. *Acta Phys. Sin.* 13, 389–398.
- Tsai, S.T., 2022. Sedimentation motion of sand particles in moving water (I): The resistance on a small sphere moving in non-uniform flow. *Theor. Appl. Mech. Lett.* 12, 100392.
- Uhlmann, M., 2005. An immersed boundary method with direct forcing for the simulation of particulate flows. *J. Comput. Phys.* 209, 448–476.
- Uhlmann, M., 2008. Interface-resolved direct numerical simulation of vertical particulate channel flow in the turbulent regime. *Phys. Fluids* 20, 053305.
- Verzicco, R., 2023. Immersed boundary methods: Historical perspective and future outlook. *Ann. Rev. Fluid Mech.* 55, 129–155.
- Vowinkel, B., Jain, R., Kempe, T., Fröhlich, J., 2016. Entrainment of single particles in a turbulent open-channel flow: A numerical study. *J. Hydraul. Res.* 54, 158–171.

- Vowinckel, B., Kempe, T., Fröhlich, J., 2014. Fluid–particle interaction in turbulent open channel flow with fully-resolved mobile beds. *Adv. Water Res.* 72, 32–44.
- Vowinckel, B., Withers, J., Luzzatto-Fegiz, P., Meiburg, E., 2019. Settling of cohesive sediment: particle-resolved simulations. *J. Fluid Mech.* 858, 5–44.
- Vowinckel, B., Zhao, K., Zhu, R., Meiburg, E., 2023. Investigating cohesive sediment dynamics in open waters via grain-resolved simulations. *Flow* 3, E24.
- Vreman, A.W., 2016. Particle-resolved direct numerical simulation of homogeneous isotropic turbulence modified by small fixed spheres. *J. Fluid Mech.* 796, 40–85.
- van Wachem, B., Elmostikawy, H., Chéron, V., 2024. Microstructure-based prediction of hydrodynamic forces in stationary particle assemblies. *Int. J. Multiph. Flow* 175, 104815.
- Wang, J., 2009. A review of Eulerian simulation of Geldart A particles in gas-fluidized beds. *Ind. Eng. Chem. Res.* 48, 5567–5577.
- Wang, L.P., Stock, D.E., 1992. Stochastic trajectory models for turbulent diffusion: Monte Carlo process versus Markov chains. *Atmos. Environ.* 26, 1599–1607.
- Wang, P., Lei, Y., Zhu, Z., Zheng, X., 2023. Drag model of finite-sized particle in turbulent wall-bound flow over sediment bed. *J. Fluid Mech.* 964, A9.
- Wang, Q., Squires, K.D., 1996. Large eddy simulation of particle-laden turbulent channel flow. *Phys. Fluids*, 8, 1790–1801.
- Wang, S., Vanella, M., Balaras, E., 2019. A hydrodynamic stress model for simulating turbulence/particle interactions with immersed boundary methods. *J. Comput. Phys.* 382, 240–263.
- Wang, S., Zhang, X., 2011. An immersed boundary method based on discrete stream function formulation for two- and three-dimensional incompressible flows. *J. Comput. Phys.* 230, 3479–3499.
- Xia, Y., Lin, Z., Guo, Y., Yu, Z., 2023. Models of interphase drag force from direct numerical simulations of upward turbulent particle-laden channel flows. *Powder Technol.* 428, 118794.
- Xia, Y., Lin, Z., Guo, Y., Yu, Z., 2024. Modelling of filtered drag force for clustered particle-laden flows based on interface-resolved simulation data. *J. Fluid Mech.* 998, A57.
- Xia, Y., Yu, Z., Pan, D., Lin, Z., Guo, Y., 2022. Drag model from interface-resolved simulations of particle sedimentation in a periodic domain and vertical turbulent channel flows. *J. Fluid Mech.* 944, A25.
- Yu, Z., Shao, X., 2007. A direct-forcing fictitious domain method for particulate flows. *J. Comput. Phys.* 227, 292–314.
- Yu, Z., Shao, X., 2010. Direct numerical simulation of particulate flows with a fictitious domain method. *Int. J. Multiph. Flow* 36, 127–134.
- Yu, Z., Xia, Y., Guo, Y., Lin, J., 2021. Modulation of turbulence intensity by heavy finite-size particles in upward channel flow. *J. Fluid Mech.* 913, A3.
- Zeng, L., Balachandar, S., Fischer, P., Najjar, F., 2008. Interactions of a stationary finite-sized particle with wall turbulence. *J. Fluid Mech.* 594, 271–305.
- Zeng, L., Najjar, F., Balachandar, S., Fischer, P., 2009. Forces on a finite-sized particle located close to a wall in a linear shear flow. *Phys. Fluids* 21.
- Zhang, Y., Jiang, M., Chen, X., Yu, Y., Zhou, Q., 2020. Modeling of the filtered drag force in gas–solid flows via a deep learning approach. *Chem. Eng. Sci.* 225, 115835.
- Zhou, Q., Fan, L.S., 2014. A second-order accurate immersed boundary-lattice boltzmann method for particle-laden flows. *J. Comput. Phys.* 268, 269–301.
- Zhou, Q., Fan, L.S., 2015a. Direct numerical simulation of low-Reynolds-number flow past arrays of rotating spheres. *J. Fluid Mech.* 765, 396–423.
- Zhou, Q., Fan, L.S., 2015b. Direct numerical simulation of moderate-Reynolds-number flow past arrays of rotating spheres. *Phys. Fluids* 27, 073306.
- Zhou, Z., Wang, S., Jin, G., 2018. A structural subgrid-scale model for relative dispersion in large-eddy simulation of isotropic turbulent flows by coupling kinematic simulation with approximate deconvolution method. *Phys. Fluids* 30, 105110.
- Zhou, Z., Wang, S., Yang, X., Jin, G., 2020. A structural subgrid-scale model for the collision-related statistics of inertial particles in large-eddy simulations of isotropic turbulent flows. *Phys. Fluids* 32, 095103.
- Zhu, Z., Hu, R., Lei, Y., Shen, L., Zheng, X., 2022. Particle resolved simulation of sediment transport by a hybrid parallel approach. *Int. J. Multiph. Flow* 152, 104072.

**Table 4**

Simulation parameters: particle Reynolds number  $Re_p = U_0 D_p / \nu$ ; turbulent intensity  $I = u_{rms} / U_0$ ; particle-to-turbulence scale ratio  $D_p / \eta$ ; turbulence-velocity-based particle Reynolds number  $Re'_p = u_{rms} D_p / \nu$ ; Taylor-microscale-based Reynolds number  $Re_\lambda = u_{rms} \lambda / \nu$ ;  $R^2(C'_D)$  and  $R^2(C'_L)$ , the coefficient of determination between the PDF of the fluctuating drag and lateral force coefficients and a normal distribution, where the mean and variance of the normal distribution are derived from the statistical properties of these force coefficients.

Method	$Re_p$	$I$	$D_p / \eta$	$Re'_p$	$Re_\lambda$	$R^2(C'_D)$	$R^2(C'_L)$	$N_x \times N_y \times N_z$	$h / \eta$
PRDNS	1	10	4.5	10	19	0.995	0.996	$400 \times 200 \times 200$	0.22
	1	20	7.1	20	30	0.998	0.997	$400 \times 200 \times 200$	0.36
	10	0.2	1.6	2	6	0.956	0.984	$400 \times 200 \times 200$	0.08
	10	0.35	2.2	3.5	10	0.978	0.995	$400 \times 200 \times 200$	0.11
	10	0.5	2.8	5	12	0.982	0.995	$400 \times 200 \times 200$	0.14
	10	1	4.5	10	19	0.983	0.986	$400 \times 200 \times 200$	0.22
	10	2.5	8.3	25	35	0.994	0.995	$400 \times 200 \times 200$	0.42
	10	5	13.6	50	52	0.991	0.996	$400 \times 200 \times 200$	0.71
	10	20	37.0	200	114	0.990	0.993	$400 \times 200 \times 200$	1.85
	40	0.2	3.9	8	16	0.985	0.997	$400 \times 200 \times 200$	0.20
	40	0.35	5.6	14	24	0.992	0.998	$400 \times 200 \times 200$	0.28
	40	0.5	7.1	20	31	0.977	0.986	$400 \times 200 \times 200$	0.35
	40	1	11.5	40	47	0.987	0.994	$400 \times 200 \times 200$	0.58
	40	5	36.9	200	114	0.985	0.990	$400 \times 200 \times 200$	1.58
	100	0.1	4.9	10	16	0.979	0.990	$400 \times 200 \times 200$	0.25
	100	0.2	7.1	20	30	0.983	0.994	$400 \times 200 \times 200$	0.36
	100	0.35	10.5	35	43	0.982	0.998	$400 \times 200 \times 200$	0.52
	100	0.5	13.5	50	53	0.989	0.998	$400 \times 200 \times 200$	0.68
	100	1	22.2	100	79	0.994	0.993	$400 \times 200 \times 200$	1.11
	100	5	76.9	500	164	0.989	0.979	$800 \times 400 \times 400$	1.92
	200	0.1	7.8	20	26	0.989	0.993	$400 \times 200 \times 200$	0.19
	200	0.2	11.7	40	46	0.995	0.994	$400 \times 200 \times 200$	0.29
	200	0.35	17.2	70	64	0.985	0.996	$400 \times 200 \times 200$	0.43
	200	0.5	22.4	100	77	0.990	0.990	$400 \times 200 \times 200$	0.56
	300	0.1	10.3	30	33	0.988	0.989	$400 \times 200 \times 200$	0.26
	300	0.2	15.6	60	57	0.988	0.993	$400 \times 200 \times 200$	0.39
	300	0.35	23.1	105	80	0.967	0.991	$400 \times 200 \times 200$	0.58
	300	0.5	30.0	150	97	0.989	0.987	$400 \times 200 \times 200$	0.75
PPDNS	0.1	10	0.35	1	31	0.998	0.999	$400 \times 200 \times 200$	0.18
	0.1	20	0.71	2	31	0.995	0.998	$400 \times 200 \times 200$	0.35
	0.2	20	0.73	4	117	0.992	0.995	$400 \times 200 \times 200$	1.82
	0.4	5	0.89	2	20	0.994	0.993	$400 \times 200 \times 200$	0.11
	0.4	10	0.70	4	127	0.990	0.997	$800 \times 400 \times 400$	1.75
	0.5	5	0.67	2.5	54	0.997	0.999	$400 \times 200 \times 200$	0.34
	0.6	2.5	0.49	1.5	36	0.998	0.998	$400 \times 200 \times 200$	0.21
	0.8	2.5	0.97	2	16	0.987	0.993	$400 \times 200 \times 200$	0.03
	0.8	5	0.73	4	117	0.991	0.989	$400 \times 200 \times 200$	1.82
	1	1	0.44	1	20	0.987	0.995	$400 \times 200 \times 200$	0.22
	1	1	0.22	1	77	0.991	0.999	$400 \times 200 \times 200$	1.12
	1.2	5	0.99	6	143	0.983	0.990	$800 \times 400 \times 400$	2.05
	2.5	0.5	0.34	1.25	52	0.991	0.999	$400 \times 200 \times 200$	0.68
	2.8	1	0.80	2.8	48	0.982	0.997	$400 \times 200 \times 200$	0.57
	3.2	0.5	0.56	1.6	32	0.980	0.999	$400 \times 200 \times 200$	0.35